Title
Nuclear Import Receptor Inhibits Phase Separation of FUS through Binding to Multiple Sites

Journal
Cell, 173(3)

ISSN
0092-8674

Authors
Yoshizawa, Takuya
Ali, Rustam
Jiou, Jenny
et al.

Publication Date
2018-04-01

DOI
10.1016/j.cell.2018.03.003

Peer reviewed

HHS Public Access

Author manuscript

Cell. Author manuscript; available in PMC 2019 April 19.

Published in final edited form as:

Cell. 2018 April 19; 173(3): 693–705.e22. doi:10.1016/j.cell.2018.03.003.

Nuclear import receptor inhibits phase separation of FUS through binding to multiple sites

Takuya Yoshizawa[1,7], **Rustam Ali**[2,7], **Jenny Jiou**[1], **Ho Yee Joyce Fung**[1], **Kathleen A. Burke**[3], **Seung Joong Kim**[4], **Yuan Lin**[2,5], **William B. Peeples**[2,5], **Daniel Saltzberg**[4], **Michael Soniat**[1], **Jordan M. Baumhardt**[1], **Rudolf Oldenbourg**[6], **Andrej Sali**[4], **Nicolas L. Fawzi**[3], **Michael K. Rosen**[2,5,*], and **Yuh Min Chook**[1,5,8,*]

[1]Department of Pharmacology, University of Texas Southwestern Medical Center, Dallas, TX 75390, USA

[2]Department of Biophysics and Howard Hughes Medical Institute, University of Texas Southwestern Medical Center, Dallas, TX 75390, USA

[3]Department of Molecular Pharmacology, Physiology and Biotechnology, Brown University, Providence, RI 02912, USA

[4]Department of Bioengineering and Therapeutic Sciences, Department of Pharmaceutical Chemistry, California Institute for Quantitative Biosciences, University of California, San Francisco, San Francisco, CA 94158, USA

[5]Howard Hughes Medical Institute (HHMI) Summer Institute, Marine Biological Laboratory, Woods Hole, MA 02543, USA

[6]Marine Biological Laboratories, 7 MBL Street, Woods Hole, MA 02543, USA

Summary

Liquid-liquid phase separation (LLPS) is believed to underlie formation of biomolecular condensates, cellular compartments that concentrate macromolecules without surrounding membranes. Physical mechanisms that control condensate formation/dissolution are poorly understood. The RNA-binding protein Fused in Sarcoma (FUS) undergoes LLPS *in vitro* and associates with condensates in cells. We show that the Importin Karyopherin-β2/Transportin-1 inhibits LLPS of FUS. This activity depends on tight binding of Karyopherin-β2 to the C-terminal

[*]Correspondence: yuhmin.chook@utsouthwestern.edu, michael.rosen@utsouthwestern.edu.
[7]These authors contributed equally
[8]Lead Contact

Declaration of Interests

The authors declare no conflict of interest.

Author Contributions

Conceptualization, Y.M.C. and M.K.R.; Methodology, Y.M.C, M.K.R., N.L.F., A.S., R.O., T.Y., R.A.; Investigation, T.Y., R.A., J.J., H.Y.J.F., Y.M.C., M.K.R., K.A.B., Y.L., W.B.P., S.J.K., D.S., M.S., J.M.B., R.O. and N.L.F.; Writing – Original Draft, Y.M.C., M.K.R., Y.L., S.J.K. and N.L.F.; Writing – Review & Editing, Y.M.C., M.K.R., T.Y., R.A.; Funding Acquisition, Y.M.C., M.K.R., R.O., A.S. and N.L.F.

proline-tyrosine nuclear localization signal (PY-NLS) of FUS. NMR analyses reveal weak interactions of Karyopherin-β2 with sequence elements and structural domains distributed throughout the entirety of FUS. Biochemical analyses demonstrate that most of these same regions also contribute to LLPS of FUS. The data lead to a model where high-affinity binding of Karyopherin-β2 to the FUS PY-NLS tethers the proteins together, allowing multiple, distributed weak intermolecular contacts to disrupt FUS self-association, blocking LLPS. Karyopherin-β2 may act analogously to control condensates in diverse cellular contexts.

Graphical abstract

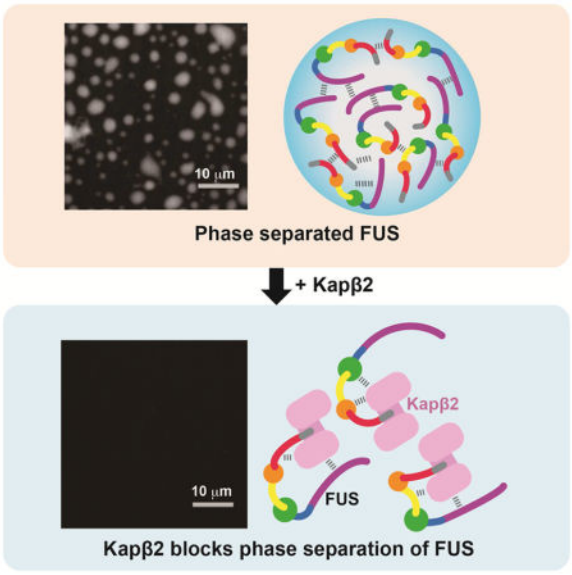

Keywords

Karyopherin-β2; Transportin-1; PY-NLS; FUS; phase separation; liquid-liquid phase separation; biomolecular condensates; low-complexity sequences; Ran GTPase; M9M; RRM; RGG; zinc finger

Introduction

The RNA-binding protein Fused in Sarcoma (FUS) plays roles in transcription, RNA processing and DNA repair (Ederle and Dormann, 2017). FUS is localized primarily to the nucleus but is also found in cytoplasmic RNP granules (Crozat et al., 1993; Ryu et al., 2014). Heat shock and DNA damage promote localization of the protein to cytoplasmic and nuclear puncta (Patel et al., 2015). FUS is involved in diverse diseases including cancer and the neurodegenerative diseases amyotrophic lateral sclerosis (ALS) and frontotemporal lobar degeneration (FTLD) (Harrison and Shorter, 2017; Schwartz et al., 2015). In ALS, FUS is often mutated in its proline-tyrosine nuclear localization sequence (PY-NLS). These alterations decrease affinity for the nuclear import factor Karyopherin-β2 (Kapβ2; also known as Transportin-1) leading to aberrant cytoplasmic localization and enrichment in RNP granules (Dormann and Haass, 2011; Zhang and Chook, 2012). Proper

compartmentalization of FUS is important in maintaining cellular homeostasis, as the degree of FUS mislocalization correlates with ALS onset and severity (Dormann and Haass, 2011).

FUS is composed of multiple structural and functional elements. It has an N-terminal disordered region with low amino acid sequence complexity that is enriched in Gly, Ser, Tyr and Gln residues (LC region), followed by a segment with Arg-Gly-Gly motifs (RGG1), a folded RNA Recognition Motif (RRM) domain, two additional RGG regions (RGG2 and RGG3) flanking a zinc-finger (ZnF) domain, and a C-terminal 26-residue PY-NLS (Figure 1A) (Ederle and Dormann, 2017). FUS is highly prone to self-association, a process that can lead to different material states including phase separated liquids, amyloid fiber containing hydrogels and aggregated solids (Burke et al., 2015; Kato et al., 2012; Murakami et al., 2015; Sun et al., 2011). The LC region undergoes liquid-liquid phase separation (LLPS) at high concentrations, through weak and transient homotypic interactions (Burke et al., 2015; Lin et al., 2015). Full-length FUS also undergoes LLPS, but at much lower concentrations, consistent with previous reports that the RGG regions can contribute to self-association of the protein (Patel et al., 2015; Sun et al., 2011). RNA enhances these processes (Burke et al., 2015; Schwartz et al., 2013). Phase separation of FUS and other disordered proteins is driven by a variety of interaction types including charge-charge, cation-π, π-π stacking and hydrogen bonds, involving side chains and backbone (Banani et al., 2017; Brangwynne et al., 2015). Over time, phase separated FUS droplets mature to more solid hydrogels that contain amyloid-like fibers (Burke et al., 2015; Kato et al., 2012; Lin et al., 2015; Murakami et al., 2015; Patel et al., 2015). Disease-causing mutations accelerate maturation of FUS droplets *in vitro* (Murakami et al., 2015; Patel et al., 2015). A recent solid state NMR analysis of fibers formed by the FUS LC region revealed a β-strand-containing structured core spanning residues 39–95, whose formation also appears to contribute to LLPS (Murray et al., 2017). Similar LLPS and maturation behaviors have been observed for other RNA binding proteins containing disordered or LC regions (Lin et al., 2015; Molliex et al., 2015; Xiang et al., 2015). The progression from phase separated liquid to a more static solid is likely controlled in cells to produce structures of different material properties, according to specific cellular needs. However the biological factors that can control self-association, LLPS and fiber formation of FUS are not known.

The FUS PY-NLS and its ALS-associated mutations seem to play no direct role in FUS self-association (Ju et al., 2011; Sun et al., 2011). However, FUS PY-NLS binding to Kapβ2 controls nuclear-cytoplasmic localization of FUS and cytoplasmic concentrations of FUS likely controls self-association and disease onset (Dormann and Haass, 2011). Kapβ2 is also the only high-affinity binding partner of FUS that has been characterized to date (Zhang and Chook, 2012). Although it is well established that Kapβ2 imports FUS into the nucleus, it is not known if Kapβ2 binding directly affects FUS self-association and/or its ability to undergo LLPS.

Here, we show that Kapβ2 inhibits LLPS of FUS, in a manner dependent on interactions with the FUS PY-NLS. The Importin-α•Importin-β (Impα/β) heterodimer and the yeast Kap121, can also inhibit FUS LLPS when the FUS PY-NLS is replaced with the appropriate cognate NLSs. Thus, Importins may generally be able to control LLPS of self-associating RNA-binding proteins through high-affinity binding to their NLSs. NMR analyses reveal

multiple weak interactions of Kapβ2 with both folded and disordered regions across FUS. Deletion or mutation of some of these elements (LC, RGG2 and RGG3) also decreases phase separation of FUS. Together, the data suggest that high-affinity interactions between Kapβ2 and the PY-NLS of FUS anchor the two proteins together, facilitating multiple weak interactions with FUS regions that mediate self-association, thus blocking phase separation. These effects may enable Kapβ2, and perhaps other Importin family members, to control the stability and dynamics of RNA-containing biomolecular condensates.

Results

Kapβ2 prevents and reverses turbidity of FUS solutions

Purified bacterially expressed Maltose Binding Protein-FUS fusion protein (MBP-FUS) is soluble and monomeric by gel filtration chromatography. The protein is polydisperse in dynamic light scattering experiments, however, suggesting the presence of minor high molecular weight oligomers (Figure S1A). The PY-NLS of FUS binds the 100 kDa Kapβ2 with dissociation constant (K_D) of 70 nM (Figure S1B). MBP-FUS also binds Kapβ2 stably, but the affinity is difficult to quantify because of the polydispersity of MBP-FUS. An approximate K_D determined by isothermal titration calorimetry (ITC) is 160 nM (Figure S1B). Addition of Kapβ2 to MBP-FUS drastically reduced polydispersity. The majority of MBP-FUS•Kapβ2 behaves as a single species, most likely the heterodimer (Figure S1C), suggesting that Kapβ2 can disrupt self-association of FUS.

Removal of MBP from MBP-FUS with the Tev protease causes FUS to self-associate, producing a turbid solution (Figure 1B and S1D, E). Addition of equimolar Kapβ2 prior to Tev cleavage prevents turbidity, consistent with formation of soluble Kapβ2•FUS heterodimer (Figure 1B, C and S1C). The ability of Kapβ2 to prevent turbidity is abolished by the M9M peptide inhibitor or the Ran GTPase (Figure 1C), which both displace cargos from Kapβ2 (Cansizoglu et al., 2007; Chook and Blobel, 1999). Kapβ2Δloop mutant, which can bind both RanGTP and PY-NLS simultaneously (Chook et al., 2002), retains the ability to block turbidity even in the presence of RanGTP (Figure 1C). Together, these data show that the ability of Kapβ2 to inhibit turbidity of FUS solutions is dependent on binding to the C-terminal PY-NLS of FUS, the same interaction that mediates nuclear import of FUS. Analogous behavior is also observed when Kapβ2 is added 60 minutes after turbidity is induced by Tev addition (Figure 1D and S1F). Thus, Kapβ2 can both inhibit and reverse turbidity caused by FUS self-association.

Kapβ2 inhibits liquid-liquid phase separation of FUS

We examined turbid solutions of fluorescently labeled FUS (5 μM MBP-FUS doped with 0.5 μM fluorescent MBP-FUS-SNAP$^{\text{SNAP-Surface 649}}$) in the presence of Kapβ2 and its regulators using spinning disc confocal microscopy (Figure 1E, F and S1G). As previously reported (Burke et al., 2015; Monahan et al., 2017; Patel et al., 2015), after removal of MBP, FUS concentrates into phase separated liquid droplets. When analyzed by polarized light microscopy, the interiors of FUS droplets show no molecular order on 350 nm length scale, consistent with them being a homogeneous liquid phase (Figure S1H). FUS droplets fuse with each other and by 24 hours accumulate into large mats of phase-separated liquid

(Figure 1E, S1G and Supplementary movie 1). As in the turbidity assays above, Kapβ2 can block phase separation of FUS and this activity is inhibited by both RanGTP and the M9M inhibitor (Figure 1E and S1G). Further, Kapβ2 can disrupt phase separated FUS droplets when added at either one hour or 48 hours after Tev addition, although clearance of droplets takes longer in the latter case (Figure 1F, Supplementary movies 2 and 3).

Other Importins can also prevent FUS LLPS if their cognate NLS is present

We next examined whether two other Importins with distinct cargo recognition sequences, the Impα/β heterodimer and the *S. cerevisiae* Importin Kap121, can also bind FUS and block its LLPS. Cognate cargo recognition sequences for Impα/β and Kap121 are the classical NLS (cNLS) and the isoleucine-lysine NLS (IK-NLS), respectively (Soniat and Chook, 2016). Initially we examined interactions of immobilized GST-Kapβ2, GST-Impα•Impβ and GST-Kap121 with MBP-FUS in pull-down binding and turbidity assays. We found that GST-Kapβ2 binds well to MBP-FUS but GST-Impα•Impβ does not (Figure S2A), consistent with Impα/β not affecting FUS turbidity (Figure 2A). In contrast, GST-Kap121 binds weakly to MBP-FUS (MBP-FUS band sub-stoichiometric to GST-Kap121 band; Figure S2A), and Kap121 partially prevents FUS turbidity (Figure 2A). When bound to IK-NLS, Kap121 no longer affects FUS turbidity suggesting that Kap121 likely uses its cargo-binding site to bind FUS weakly (Figure 2A).

To learn whether the lack of activity of Impα/β could be due simply to low affinity for FUS, we replaced the PY-NLS in FUS (residues 501–526) with a high affinity cNLS to give FUS(cNLS). Pull-down binding assays showed that MBP-FUS(cNLS) binds both Impα alone and Impα/β, consistent with direct binding to Impα, as observed for all known Impα/β cargos (Figure S2A). In turbidity assays, Impα alone had no effect on FUS(cNLS) turbidity, but Impα/β blocked turbidity in a RanGTP-sensitive manner (Figure 2B). We also replaced the PY-NLS of FUS with an IK-NLS to give FUS(IK-NLS) (Kobayashi and Matsuura, 2013). Analogous to the results above, LLPS of this chimera is strongly inhibited by Kap121 in a RanGTP-sensitive manner (Figure 2C). In summary, when FUS has an appropriate high-affinity recognition signal, an Importin family member that is distinct from Kapβ2 can block its phase-separation. This inhibition requires a β-Importin family member as Impα alone has no effect.

Kapβ2 is unlikely to act non-specifically to disrupt LLPS

Previous studies reported that FUS PY-NLS does not participate directly in FUS self-association (Ju et al., 2011; Sun et al., 2011). It is therefore unclear how Kapβ2 binding to this element could block LLPS by FUS. One limiting possibility is that simply tethering any large molecule to the C-terminus of FUS may act non-specifically to alter the balance between FUS-FUS and FUS-solvent interactions, disfavoring the former and thus inhibiting LLPS. Alternatively, Kapβ2 may be acting specifically, through binding competitively to regions of FUS that mediate self-association.

To examine the former possibility, we replaced the FUS PY-NLS with a high-affinity nuclear export signal (NES) to generate a FUS(NES) chimera (Ohshima et al., 1999). In contrast to the FUS(cNLS) and FUS(IK-NLS) chimeras, phase separation of FUS(NES) was not

inhibited by its cognate Kapβ protein, the 127 kDa Exportin CRM1/XPO1 (Figure 2D) even though the two proteins bind each other tightly (Figure S2A). Similarly as described above, the 60 kDa Impα does not disrupt LLPS of FUS(cNLS) (Figure 2B and S2A). Thus merely tethering large proteins to the FUS C-terminus is insufficient to inhibit LLPS.

We recently showed that tethering self-attractive proteins to a phase-separating system increases the drive to phase separate and tethering self-repulsive proteins has an opposite effect (Lin et al., 2017). To investigate whether Kapβ2 has attractive or repulsive self-interactions, we measured its diffusion interaction parameter, κ_D; positive κ_D suggests net repulsive interactions and negative κ_D indicates net attractive interactions (Connolly et al., 2012). As shown in Figure 2E, Kapβ2 has $\kappa_D = -173$ ml/g, indicating attractive self-interactions. Thus, the protein is unlikely to act non-specifically to generate repulsion between FUS molecules.

Kapβ2 interacts weakly and non-uniformly with residues in FUS LC

FUS is believed to phase separate due to weak homotypic interactions involving the LC region and C-terminal elements (Burke et al., 2015; Monahan et al., 2017; Patel et al., 2015). Kapβ2 could block phase separation by competitively binding these elements, which are outside of the PY-NLS. The affinities of Kapβ2 for full-length FUS and the FUS PY-NLS are similar (K_D ~160 nM *vs.* ~70 nM) suggesting that such additional interactions are likely weak (Figure S1B). The lack of stable Kapβ2•FUS contacts outside the PY-NLS is consistent with observations that only the PY-NLS is observed in crystal structures of Kapβ2 bound to FUS (full-length), FUS(371–526) and FUS(456–526) (crystallographic statistics in Table S1; ITC analysis, structures and electron density maps shown in Figure S2B–H).

We used NMR spectroscopy to identify regions of FUS outside its C-terminal PY-NLS that contact Kapβ2 (Figure 3A–B, 4A–E and 5A–E). β-Importin proteins make many weak and highly dynamic interactions with phenylalanine-glycine (FG) repeats in various nucleoporins to traverse the nuclear pore complex (Hough et al., 2015; Milles et al., 2015). The FUS LC (residues 1–163) contains 24 motifs with the sequence [S/G]Y[S/G] (Figure 3A–B and S3A–B), potentially analogous to the FG repeats in the nuclear pore complex. Thus, we initially analyzed $^{1}H/^{15}N$ HSQC spectra of ^{15}N-FUS LC in the absence and presence of Kapβ2 to identify such contacts (Figure 3A and S3A). At conditions where FUS LC is not phase separated (75 μM, 10 °C), many resonances progressively shift and decrease in intensity as Kapβ2 is increased from 0 to 112.5 μM (Figure 3B; chemical shift assignments from (Burke et al., 2015)). These behaviors are consistent with weak binding that is not saturated at these conditions. The attenuation/shifting of FUS LC resonances is distributed non-uniformly across the protein. The largest perturbations are observed for resonances from the segments ^{37}SYSGY^{41}, ^{97}YPGY^{100} and ^{149}YSPPSG^{154}, suggesting relatively stronger binding to these elements (Figure 3B and Figure S3B). The ^{37}SYSGY^{41} is part of the β-strand-containing structured core observed in solid state NMR analysis of LC fibers (Murray et al., 2017), suggesting that disruption of the core may contribute to the effects of Kapβ2. Amide resonances change similarly upon addition of Kapβ2 alone or Kapβ2•PY-NLS, indicating contacts outside the PY-NLS binding site of the karyopherin (Figure S3B).

Kapβ2 interacts weakly with folded and disordered regions within FUS(164–500)

Beyond the LC region, C-terminal elements also contribute to LLPS of FUS (Burke et al., 2015; Monahan et al., 2017). Thus, we next examined interactions of FUS(164–500) with Kapβ2. Because of the complex nature of this fragment, containing two folded domains surrounded by three intrinsically disordered elements, we used NMR cross saturation transfer experiments to look for regions that directly contact Kapβ2. In these experiments, $^{15}N/^{2}H$ labeled FUS(164–500) (protonated at amide positions, deuterated at all aliphatic sites) is mixed with fully protonated Kapβ2. Irradiation of such samples in the aliphatic region of the spectrum saturates resonances of Kapβ2 and this saturation is transferred to amides of FUS that are in direct contact with the Karyopherin. Saturation is manifest as decreases in intensity of selected amide resonances in FUS, which are observed in HSQC-type $^{1}H/^{15}N$ correlation spectra. The experiment can be complicated by the dynamics of the interactions, such that decreases at *bona fide* interfaces may not be observed if the bound populations are low or interaction kinetics are in the wrong rate regime (Jayalakshmi and Krishna, 2002; Ueda et al., 2014). The data can be particularly complicated in interactions of disordered proteins, where different parts of the chain may contact a partner with different local dynamics.

Addition of Kapβ2 to ^{15}N-FUS(164–526) harboring the PY-NLS causes severe line-broadening of most resonances in $^{1}H/^{15}N$ HSQC spectra, including all of those representing the folded domains and much of the disordered regions thus precluding analysis (Figure S4A). This broadening probably occurs because of the large size of the FUS•Kapβ2 complex (~160 kDa) and slow exchange between the bound and free states arising from the high-affinity interaction. Thus, to weaken the interactions and identify direct Kapβ2 contact sites we recorded spectra on $^{15}N/^{2}H$-FUS(164–500) lacking the PY-NLS, in the presence of Kapβ2 bound to the pM affinity M9M peptide inhibitor (to exclude artifactual contacts to the PY-NLS binding site, which would be occluded in the native FUS•Kapβ2 complex).

The $^{1}H/^{15}N$ HSQC spectrum of 17 μM ^{15}N-FUS(164–500) shows many strong resonances with ^{1}H chemical shifts between ~7.5 ppm and 8.5 ppm, mostly representing residues in unstructured regions of the protein, as well as numerous resonances outside of this window, which represent the folded RRM (residues 285–370) and Cys4-type ZnF (residues 421–455) domains (Figure S4B and Tables S2, S3). Correspondence between the dispersed resonances and reported chemical shift assignments of the two domains (Iko et al., 2004; Liu et al., 2013) enabled us to assign most resonances from the RRM and ZnF to specific residues (Figure S4B, Figure 4A, C).

In cross saturation transfer experiments, minimal changes were observed in amide resonances of $^{15}N/^{2}H$-labeled FUS(164–500) alone (not shown). In the presence of 1.5-fold excess Kapβ2•M9M, a subset of amide resonances in the RRM domain showed particularly large decreases in intensity (> 60%; Figure 4A, D). These resonances mapped to a contiguous patch on one face of the FUS RRM domain (PDBID 2LCW; (Liu et al., 2013)) defined by its two α-helices (Figure 4B). Similarly we observed greater decreases in intensity (> 45%) of certain resonances in the ZnF domain (Figure 4C, D). These resonances mapped to one face of a homology model of the FUS ZnF (PDBID **2K1P**; (Iko et al., 2004;

Loughlin et al., 2009)), defined by its C-terminal β-strand (Figure 4E). Although the uncertainties in intensity ratio (saturated vs unsaturated) for any individual peak is relatively large due to the broad lines induced by Kapβ2, the convergence of the affected residues to contiguous patches affords confidence that they map contact sites on the RRM and ZnF domains.

As in our analysis of the LC region, we also examined line broadening of FUS resonances upon addition of 3-fold excess Kapβ2•M9M. As detailed in Figures S4C-G, similar, although more extensive, regions of the RRM and ZnF domains were also perturbed by Kapβ2 addition in these experiments. Thus, the cross saturation transfer and line broadening data indicate that in the absence of high-affinity Kapβ2-PY-NLS binding, the RRM and ZnF domains can make weak direct contacts to regions of the Karyopherin outside of its PY-NLS binding site.

Analysis of the unfolded RGG regions of FUS(164–500) was complicated by the low sequence complexity of these elements, which produces severe overlap in $^{1}H/^{15}N$ correlation spectra. Of the 146 glycine residues in the three regions, only 30 distinct peaks could be observed in the glycine region of the spectra (105–111 ^{15}N ppm) (Figure 5A). The glycine resonances appear to be present but overlapped, rather than absent due to line broadening, based on spectra of fragments containing individual RGG elements (RGG1 alone, RGG2-ZnF and ZnF-RGG3). That is, there are many instances of peaks with identical chemical shifts appearing in spectra of different fragments, and the fragment spectra are largely subsets of the FUS(164–500) spectrum (Figure S5A–D and 5A-F). In cross saturation transfer experiments of $^{15}N/^{2}H$-FUS(164–500) plus excess Kapβ2•M9M, only one of the 30 distinct glycine peaks, peak 8, decreased (Figure 5F). This peak could be assigned to RGG3 based on comparison to spectra of the fragments (Figure S5D).

In line broadening experiments, several glycine peaks in FUS(164–500) decreased in intensity upon addition of excess Kapβ2 (Figure 5A). Comparison to the RGG fragments allowed some of these to be assigned to RGG2 and others to RGG3 (Figure 5A and S5C, D). In analogous experiments involving the RGG2-ZnF and ZnF-RGG3 fragments, these same peaks plus others broadened upon Kapβ2 addition (Figure 5C, D). In spectra of these fragments and of FUS(164–500), the chemical shifts of ZnF resonances are identical within experimental error to those of the isolated domain (Figure S5F), suggesting that there are no intramolecular contacts of the RGG regions with the ZnF domain (see Figure S5F legend for a more detailed discussion). Thus, the line broadening most likely represents direct Kapβ2 binding to RGG2 and RGG3. RGG1 may also make direct contacts, based on line broadening observed in spectra of isolated RGG1 plus Kapβ2•M9M (Figure 5B), although this is less certain since RGG1 resonances are severely overlapped in spectra of FUS(164–500). Consistent with binding of RGG regions, a number of unassigned resonances representing non-glycine residues in the unfolded region of the spectra of FUS(164–500) also broadened upon Kapβ2 addition (Figure S5G). We note that the most severely broadened glycine peak (#8) was the same as that affected in the cross saturation transfer experiment, showing consistency between the experiments (Figure 5F). Inefficient cross saturation transfer between Kapβ2 and the RGG2/3 regions probably results from a

combination of low bound populations of individual Arg-$(Gly)_n$ or $(Gly)_n$ motifs and binding dynamics that are unfavorable to the experiment.

The combined NMR data show that Kapβ2 binds to the N-terminal LC region (Figure 3B) as well as large portions of the FUS C-terminal segment (Figure 4A–E and 5A–F), including the RGG2 and RGG3 regions, the RRM and ZnF domains.

Implications of Kapβ2 binding across FUS: SAXS analysis and RNA-binding

Small angle X-ray scattering (SAXS) analysis shows substantial compaction of full-length FUS upon binding Kapβ2. Five SAXS profiles (MBP, MBP-FUS, Kapβ2, Kapβ2•FUS and Kapβ2•MBP-FUS) were analyzed to calculate radius of gyration (R_g^{SAXS}), maximum particle size (D_{max}), and pair distribution function (P(r)) (Figure 6A) (Franke et al., 2017). According to the molecular weight estimation from SAXS analysis (Table S4), the polydispersity of MBP-FUS is highly concentration dependent. Thus, the parameters in Figure 6A were calculated from the merged SAXS profiles, where polydispersity of MBP-FUS (and other samples tested) is negligible (Kikhney and Svergun, 2015). To assess compactness of the SAXS samples, $R_g^{Globular}$ was estimated using a formula of $6.6*MW^{0.333}$ Å (for MW in kDa; (Erickson, 2009). MBP-FUS presents the largest values of $R_g^{SAXS}/R_g^{Globular}$, D_{max}, *and* D_{max}/R_g^{SAXS}, suggesting that FUS is significantly expanded/extended in solution compared to globular proteins. In contrast, Kapβ2•FUS presents smaller values of $R_g^{SAXS}/R_g^{Globular}$, D_{max}, and D_{max}/R_g^{SAXS}, suggesting that FUS becomes more compact upon binding Kapβ2. Consistently, the *ab initio* shapes computed from the experimental SAXS profiles (Figures 6A and S6A-E), as well as the pair distribution functions (Figure S6F) further support the compactness of FUS upon binding Kapβ2 (similar in buffers with 5% or 20% glycerol; Figure S6G).

The RGG regions and ZnF and RRM domains were previously shown to bind RNA. The ZnF and RRM domains bind weakly to GGUG-containing RNA, with K_D values in the micromolar range (Iko et al., 2004; Ozdilek et al., 2017). In contrast, the RGG regions bind RNA with K_D values in the nanomolar range. We examined the effects of Kapβ2 on FUS binding to two RNAs, the 48-nucleotide prD (DNMT) RNA (K_D ~0.7 μM; binds RGG1 and RGG3) and the 24-nucleotide telomeric repeat TERRA RNA (K_D ~12 nM; binds RGG3) (Ozdilek et al., 2017; Takahama and Oyoshi, 2013). Figures 6B and C show MBP-FUS binding to fluorophore-labeled prD and TERRA, respectively. Addition of Kapβ2 to the MBP-FUS•RNA complexes caused efficient release of prD, but only partial release of the higher affinity TERRA, consistent with overlapping binding sites in the FUS RGG regions. Since RNA promotes aggregation and LLPS of FUS (Burke et al., 2015; Schwartz et al., 2013), our data also suggest that Kapβ2 may inhibit biological phase separation of FUS through blocking interactions with RNA.

Regions of FUS that bind Kapβ2 contribute to LLPS

We examined the temperature dependence of LLPS of full-length FUS and a series of deletion mutants to identify functionally important regions. At 8 μM, FUS phase separates at temperatures below 33°C (cloud point temperature, T_{cloud}), as assessed by a sharp increase in turbidity when temperature is decreased slowly from 45°C (Figure 7A). Removal of the

PY-NLS did not affect LLPS (FUS(1–500) T_{cloud} 33°C; Figure 7A), consistent with observations that the PY-NLS does not affect FUS aggregation (Ju et al., 2011; Sun et al., 2011).

Our NMR data suggest that Kapβ2 contacts three segments of the FUS LC (Figure 3B and Figure S3B). Alanine mutation of the five tyrosines in these segments (Tyr38, Tyr 41, Tyr97, Tyr100 and Tyr149) in full-length FUS (FUS(Y_5A)) substantially decreased T_{cloud} to 25°C (Figure 7A), consistent with the importance of tyrosine side chains in self-assembly of the FUS LC region (Kato et al., 2012; Lin et al., 2017), and in LLPS of disordered proteins in general (Banani et al., 2017; Brangwynne et al., 2015).

Deletion of the RRM or ZnF domain (FUS(ΔRRM) or FUS(ΔZnF)) does not decrease the ability of FUS to phase-separate. The T_{cloud} of 33.6°C for FUS(ΔZnF) is similar to that of wildtype FUS, while the T_{cloud} of 38°C for FUS(ΔRRM) suggests an enhancement in phase separation (Figure 7A). As described in Figures S7A-B, S5A, B, E and 5A, enhancement of LLPS by RRM deletion appears to derive from loss of inhibitory intramolecular interactions between the domain and RGG regions (see below).

We made several mutants to perturb the FUS RGG regions. Mutating all arginine residues in RGG2 and RGG3 of full-length FUS to lysines (FUS(RtoK) decreased T_{cloud} to 23.5°C (Figure 7A) suggesting stereospecific roles of arginine side chains in promoting LLPS. The FUS(1–452) truncation mutant has a similarly low T_{cloud} of 22.5°C indicating the importance of RGG3 in LLPS (Figure 7A). The last mutant, FUS(1–370), lacks both RGG2 and RGG3 and shows a drastic decrease in its ability to phase separate (T_{cloud} of 8°C).

At 2 μM, wildtype FUS and the mutants showed the same trends in LLPS as at 8 μM, but T_{cloud} was uniformly decreased as expected from theory (Figure S7C). We also observed the same patterns in temperature-dependent analyses of LLPS by fluorescence microscopy, with FUS(ΔRRM) > FUS wildtype > FUS(1–452) in their propensity to phase separate (Figure S7D). Together, these studies show that the LC and RGGs regions are the main determinants of FUS LLPS.

As detailed below, our combined data lead to a model in which FUS is anchored to Kapβ2 through high-affinity interactions of the PY-NLS. This enables distributed weak interactions to disrupt FUS self-association and phase separation. A prediction of this model is that even in the absence of the Kapβ2-PY-NLS interactions, high concentrations of the Karyopherin should disrupt FUS phase separation. Consistent with this prediction, we found that very high concentrations (64 μM) of Kapβ2•M9M are able to inhibit phase separation of FUS(1–500), which lacks the PY-NLS (Figure 7B).

Discussion

Kapβ2 is the dominant nuclear transport factor that traffics FUS into the nucleus (Dormann and Haass, 2011). This activity is based on high-affinity, RanGTP-sensitive binding of Kapβ2 to the PY-NLS of FUS (Lee et al., 2006; Zhang and Chook, 2012). Here we describe an additional biochemical consequence of this interaction - disruption of LLPS of FUS. Mechanistic studies show that in addition to the established high affinity binding of Kapβ2

to the FUS PY-NLS, regions outside of the PY-NLS binding pocket of the karyopherin make weak, distributed interactions with multiple regions of FUS. These regions include tyrosine-repeats in the LC region, the RGG elements and the folded RRM and zinc finger domains. Of these FUS elements, the LC and RGG regions contribute to LLPS. Thus, heterotypic Kapβ2-FUS interactions should compete with homotypic FUS-FUS interactions. Since the drive for phase separation is distributed across the FUS sequence, it seems logical that Kapβ2 binds in distributed fashion to block phase separation. Our data suggest a model where high-affinity and stable tethering of Kapβ2 to the FUS PY-NLS enables weak and dynamic interactions involving other regions of the two proteins, which block formation of higher-order FUS assemblies and phase separation.

Within the complex, it is possible that Kapβ2 engages all sites on FUS simultaneously. Alternatively the complex may be dynamic in nature, sampling different collection of contacts that rapidly interconvert, as observed in other IDP interactions, for example the binding of disordered cyclin-dependent kinase (CDK) inhibitor Sic1 to its receptor Cdc4 (Mittag et al., 2008). Based on structural and energetic considerations, we favor the latter model of a dynamic complex. The regions of Kapβ2 that bind the different FUS elements remain unknown. However, features of the karyopherin that are conserved among other β-Importin proteins suggest potential modes of interaction. First, Kapβ2 possesses a series of hydrophobic patches on the convex spine of its superhelical structure (Chook and Suel, 2011; Conti and Izaurralde, 2001) (Figure S7E). During nuclear import, these patches bind in dynamic fashion to the large arrays of FG repeats in the nuclear pore complex. These same regions could be repurposed to make analogous interactions with tyrosine repeats in the FUS LC region. In addition, Kapβ2 possess highly acidic surfaces and adjacent long acidic loops on the concave side of its superhelix. Portions of these acidic elements bind to the FUS PY-NLS, but parts remain solvent-exposed in the complex (Figure S7E), and could interact with the basic RGG regions of FUS. Interactions with these spatially distributed surfaces on Kapβ2 significantly constrain the FUS chain, as evidenced by our SAXS data showing compaction of the extended FUS upon binding the karyopherin.

In addition to FUS, Kapβ2 binds and imports many PY-NLS containing, RNA-binding proteins including EWS, TAF15, hnRNP A1 and hnRNP A2. Like FUS, these proteins contain folded RNA binding domains as well as LC and RGG regions, and are found in RNA granules (King et al., 2012). As shown in the companion paper by Shorter and colleagues, high-affinity binding of Kapβ2 to the PY-NLSs of these proteins prevents their self-association and likely phase separation (Guo et al, in press). Although the Kapβ2 cargos have different domain arrangements, in all cases individual elements are either disordered or connected by flexible linkers. Thus, Kapβ2 can probably contact the RGG and LC regions of the cargos when anchored to their PY-NLSs, disrupting self-association through a mechanism analogous to that of FUS.

In addition to Kapβ2, other β-Importin family members may also act to modulate phase separation of LC-containing RNA-binding proteins. We have shown here that two other Importins can inhibit LLPS by FUS when the protein is equipped with high-affinity recognition peptides. β-Importin family members share both the hydrophobic patches on the convex spine and the acid surfaces and loops on their concave side, which are likely

important in disruption of LLPS by FUS (Chook and Suel, 2011; Conti and Izaurralde, 2001) (Figure S7E). These same elements could be used to disrupt LLPS by other RNA-binding proteins. While conceptually similar, this molecular mechanism is distinct from that proposed previously to account for the chaperone activity of Importins toward positively charged cargo proteins (Jakel et al., 2002). In contrast to Importins, Exportins such as CRM1 have very different charge distributions and spatial relationships between NES- and FG-binding sites (Dong et al., 2009; Fung and Chook, 2014; Port et al., 2015). Unlike the large contiguous negatively charged surfaces on the concave side of Importins, analogous surfaces of Exportins are basic (Figure S7E, F). Further, in contrast to NLSs, which bind the concave acidic surfaces of Importins, the NES binds in a hydrophobic groove that is located on the FG-repeats-binding convex surface of CRM1 (Figure S7E, F). Thus, conserved features enable Importins to disrupt LLPS of RNA binding proteins that possess appropriate NLSs, an activity that is likely not shared by Exportins resembling CRM1.

We can envision several potential mechanisms by which the ability of Kapβ2 to control FUS LLPS could be important in cell physiology. First, Kapβ2 may bind newly translated FUS and prevent it from phase separating in the cytoplasm while escorting it into the nucleus. Kapβ2-FUS interactions may also modulate cytoplasmic RNA granules, where FUS is localized upon heat shock or other cellular stresses (Dormann et al., 2010; Li et al., 2013; Patel et al., 2015). In this role, Kapβ2 may facilitate dissociation of FUS from RNA, controlling dynamics of the protein and/or its stoichiometry in the condensates. If FUS is important to granule stability, Kapβ2 could control granule formation and/or disassembly, as we observed here. Finally, by weakening intermolecular contacts, substoichiometric amounts of Kapβ2 could modulate the material properties of granules, likely affecting the chemistry that occurs within them (Banani et al., 2017); Guo et al and Hofweber et al in press). In conclusion, our data suggest an expanded role for β-Importins. Not only do they traffic proteins into the nucleus, they also may control the formation, composition and dynamics of biomolecular condensates.

STAR * METHODS

Contact for Reagent and Resource Sharing

Further information and requests for resources and reagents should be directed to and will be fulfilled by the Lead Contact, Yuh Min Chook (yuhmin.chook@utsouthwestern.edu).

Experimental Method and Subject Details

All recombinant proteins were expressed in BL21 (DE3) E. coli cells growing in LB medium or M9 medium.

Method Details

Constructs, protein expression and purification—Kapβ2, Kapβ2Δloop (residues 337–367 replaced with a GGSGGSG linker), Impα, Impβ, Kap121 and CRM1 were expressed as GST-fusions, which were generated by inserting PCR fragments of the gene of interest (all Karyopherins, except the *S. cerevisiae* Kap121, are human proteins) into the pGEX-TEV plasmid, which is a pGEX4T3 vector (GE Healthcare, UK) modified to include

a TEV cleavage site (Chook and Blobel, 1999). All FUS proteins were expressed from MBP-fusion constructs using the pMAL-TEV vector, which is a pMAL (New England BioLabs, Ipswich, MA) modified to contain a TEV cleavage site (Chook et al., 2002) or a pMAL-TEV vector modified to express His_6-MBP instead of MBP (p6xHisMal-TEV). FUS mutations were made by site-directed mutagenesis using a Quik-Change Site-Directed Mutagenesis Kit (Stratagene, La Jolla, CA), and all constructs were sequenced. MBP-FUS(cNLS), MBP-FUS(IK-NLS) and MBP-FUS(NES) chimeras were made by inverse PCR method. FUS residues 501–526 were replaced with either $SV40^{NLS}$ (PKKKRKV), Pho4 residues 140–166 (^{140}SANKVTKNKSNSSPYLNKRRGKPGPDS^{166}) or the NES from the NS2 protein of the MVM virus (YSTVDEMTKKFGTLTIH), respectively. A MBP-FUS-SNAP construct was generated by cloning in a SNAP tag (New England BioLabs), preceded by a TGGGS linker, at the C-terminus of MBP-FUS (full-length).

All recombinant proteins were expressed individually in BL21 (DE3) *E. coli* cells (induced with 0.5 mM isopropyl-β-d-1-thiogalactoside (IPTG) for 12 hours at 25°C for Importins and at 18°C for FUS). Bacteria expressing Importins were lysed with the EmulsiFlex-C5 cell homogenizer (Avestin, Ottawa, Canada) in buffer containing 50 mM Tris pH 7.5, 200 mM NaCl, 20% (v/v) glycerol, 2 mM DTT, 1 mM EDTA, and protease inhibitors. To purify untagged Importins, GST-Importins were first purified by affinity chromatography using GSH sepharose beads (GE Healthcare, UK), eluted, cleaved with TEV protease, and further purified by ion-exchange and gel filtration chromatography in TB buffer (20 mM HEPES pH 7.4, 200 mM NaCl, 2 mM DTT, 2 mM $Mg(OAC)_2$, 10% glycerol, 1 mM EGTA). For pull-down binding assays, affinity purified GST-Importins were eluted and then dialyzed against buffer containing 20 mM HEPES pH 7.4, 150 mM NaCl, 2 mM DTT and 10% glycerol.

Bacteria expressing MBP-FUS proteins for crystallization, turbidity, imaging and pull-down binding assays were lysed in 50 mM HEPES pH 7.4, 1.5 M NaCl, 10% glycerol, 2 mM DTT (high salt to disrupt association with nucleic acid). MBP-FUS proteins were purified by affinity chromatography using amylose resin (New England BioLabs, Ipswich, MA), eluted with buffer containing 20 mM HEPES pH 7.4, 150 mM NaCl, 2 mM DTT, 10% glycerol, and 20 mM maltose and either dialyzed extensively in final maltose-free buffers to remove maltose or further purified by ion-exchange chromatography. Purification of the MBP-FUS proteins always included either high salt or RNAse A treatment to eliminate RNA (purified proteins have A_{260}/A_{280} ratios of 0.50–0.71), and the absence of EDTA to maintain the fold of its zinc finger domain. MBP-FUS proteins are also free of maltose since they are able to be immobilized on amylose resin.

RanGTP (GSP1 residues 1–179, Q71L) and M9M was purified as previously described (Cansizoglu et al., 2007; Fung et al., 2015). *E. coli* expressed His_6-RanGTP was purified using affinity and cation exchange chromatography. Purified protein was concentrated and exchanged buffer into 20 mM HEPES pH 7.4, 100 mM sodium chloride, 4 mM magnesium acetate, 1 mM DTT, 10% Glycerol. cNLS, M9M and IK-NLS peptides were expressed as a GST-fusions, purified using GSH sepharose followed by cleavage of GST tag and further purified by gel filtration in buffer containing 20 mM HEPES pH 7.4, 150 mM NaCl, 2 mM DTT and 10% glycerol.

Turbidity Assays

FUS turbidity analysis at room temperature—Importins and its NLSs, M9M or buffer are mixed at room temperature for 30 minutes prior to turbidity assays. 8 μM MBP-FUS and buffer, 8 μM Importins (Importins, Importin•NLS or Kapβ2•M9M) ± 8 μM RanGTP were mixed in buffer containing 20 mM HEPES pH 7.4, 150 mM NaCl, 2 mM DTT, 2 mM $Mg(OAC)_2$, 10% glycerol to reaction volumes of 100 μL. TEV was added at time= 0 min to final concentration of 25 μg/mL. Absorbance at 395 nm (OD_{395nm}) was monitored at room temperature using Variskan plate reader (Thermo Fisher Scientific, Inc.).

Temperature dependent FUS turbidity analysis—Prior to tracking turbidity, 8 μM MBP-FUS proteins (in buffer containing 20 mM HEPES pH 7.4, 150 mM NaCl, 2 mM DTT, 2 mM magnesium acetate, 10% glycerol) were treated with Tev protease (final concentration 25 ug/mL Tev) in reaction volumes of 500 uL for 3 hours at room temperature, and then placed in a cuvette. OD_{395nm} was measured using a Cary 100 UV-Visible spectrophotometer equipped with a Peltier thermal controller (Agilent Technologies, Australia). FUS reaction mixtures in cuvettes were held at 45°C or 40°C for 10 min then cooled gradually at a rate of −0.5°C/min. OD_{395nm} of FUS proteins were monitored every 0.5°C. T_{Cloud} is the x-intercept of tangent at inflection point of the curve (mean of 3 technical replicates, ± S.D.).

Monitoring interactions between Importins and FUS

In vitro pull-down binding assays were performed using GST-Kapβ2, GST-Impα, GST-Impα/β or GST-Kap121 immobilized on GSH Sepharose beads. ~ 4 μM GST-Importins were immobilized on beads. 30 μL of GST-Importins beads are incubated with 8 μM MBP-FUS proteins (total 80 μg) for 30 min at room temperature and washed three times with buffer containing 20 mM HEPES pH7.4, 150 mM NaCl, 10% glycerol, 2 mM $Mg(OAC)_2$ and 2 mM DTT. Bound proteins were separated by SDS-PAGE and stained with Coomassie blue.

Gel filtration chromatography to assess complex formation was performed using a Superdex 200 10/300 GL column (GE Healthcare). 500 μL of protein samples were loaded onto the column and eluted with buffer containing 20 mM HEPES pH7.4, 150 mM NaCl, 10% glycerol, 2 mM $Mg(OAC)_2$ and 2 mM DTT. Eluted fractions were visualized by SDS-PAGE/ Coomassie Blue.

Binding affinities of MBP-FUS proteins to Kapβ2 were measured using isothermal titration calorimetry (ITC). ITC experiments were performed with a Malvern iTC200 calorimeter (Malvern Instruments, Worcestershire, UK). Proteins were dialyzed overnight against buffer containing 20 mM HEPES pH 7.4, 150 mM NaCl, 10% glycerol, and 2 mM β-mercaptoethanol. 50–100 μM MBP-FUS proteins were titrated into the sample cell containing 5–10 μM recombinant Kapβ2. ITC experiments were performed at 20°C with 19 rounds of 2 μL injections. Data were integrated using NITPIC (Scheuermann and Brautigam, 2015), globally fitted using SEDPHAT (Brautigam et al., 2016; Zhao et al., 2015), and plotted with GUSSI (Brautigam, 2015). Confidence intervals for reported K_Ds were calculated with projection method at 68.3% confidence level in SEDPHAT.

Monitoring the effects of Kapβ2 on FUS-RNA interactions

prD (5′-AUUGAGGAGCAGCAGAGAAGUUGGAGUGAAGGCAGAGAGGGGUUAAGG-3′, 48-mer) and TERRA (5′-UUAGGGUUAGGGUUAGGGUUAGGG-3′, 24-mer) were chemically synthesized (Integrated DNA Technologies, Coralville, IA). Both RNAs were 5′-end labeled with 6-FAM (Fluorescein). prD (in buffer containing 20 mM Hepes pH 7.4, 150 mM KCl, 2 mM DTT, 2 mM magnesium acetate, 10% glycerol) was heated at 95°C for 5 min and snap-cooled on ice for 10 min. TERRA in the same buffer was heated at 95°C for 5 min and cooled down to 4°C at a rate of 1°C/min for annealing on T100 thermal cycler (Bio-Rad, Hercules, CA). RNA, MBP-FUS and Kapβ2 were mixed at room temperature for at least 10 min prior to gel filtration chromatography. 1 μM prD or 2 μM TERRA ± 3 μM MBP-FUS ± 3.2 μM Kapβ2 were mixed in buffer containing 20 mM HEPES pH 7.4, 150 mM KCl, 2 mM magnesium acetate, 10% glycerol and 2 mM DTT. Gel filtration chromatography with a Superdex 200 10/300 GL column (GE Healthcare) was used to assess complex formation. 100 μL of proteins ± RNA samples were loaded onto the column and eluted with buffer containing 20 mM HEPES pH7.4, 150 mM KCl, 10% glycerol, 2 mM magnesium acetate and 2 mM DTT. Protein(s) in eluted fractions (500 μL each) were visualized by SDS-PAGE/Coomassie Blue. The RNA in each fraction was tracked by monitoring fluorescence emission at 520 nm from the 6-FAM tag (excited at 495 nm) using Varioskan plate reader (Thermo Fisher Scientific, Inc.).

Imaging of turbid FUS solution

For imaging experiments, purified MBP-FUS-SNAP was labeled with SNAP-Surface 649 fluorophore (New England BioLabs) by incubating with 5-fold excess fluorophore for 2 hours at room temperature. Unreacted fluorophore was removed by dialysis. 5 μM MBP-FUS, 0.5 μM MBP-FUS-SNAP$^{\text{SNAP-Surface 649}}$ and either buffer or 10 μM Kapβ2 ± 15 μM M9M or 15 μM RanGTP were mixed at room temperature in total volumes of 100 μL in individual wells of CultureWell non-removable chamber cover glass (Grace Bio-Labs). All wells were made up to 100 μL with buffer containing 10 mM HEPES pH7.4, 150 mM NaCl, 2 mM $Mg(OAC)_2$, 2 mM DTT and 10% glycerol. Tev protease was added to final concentration of 1.5 μM at time= 0 hr. Wells containing protein mixtures were imaged by spinning disk confocal microscopy beginning at time = 1 hr. Spinning disk confocal microscopy was executed using a Yokogawa CSU-X scanhead (Solamere Technology Group) mounted on an ASI Rapid Automated Modular Microscope system equipped with motorized XT stage and piezo z-motor in the stage (ASI), an Andor iXon Ultra 897 camera (Andor), and laser illumination using a VersaLase laser system equipped with 405, 488, 561, and 640 nm laser (Vortran Laser Technology). A multi-bandpass dichroic mirror in the Yokogawa scanhead was combined with dye specific emission filters (Chroma Technology Corp.) in a Finger Lakes Instrument filter wheel (Finger Lakes Instrument). Nikon 60x 1.4na oil immersion objective lens (Nikon) was used. The microscope system was operated using the Micro-Manager software package (http://micro-manager.org).

Polarized light microscopy was performed with the LC-PolScope, employing a liquid crystal based universal compensator to generate retardance maps that are independent of the orientation of the slow axis of birefringence (Oldenbourg, 1991; Oldenbourg and Mei,

1995). The instrument was implemented on an inverted microscope stand (Nikon Eclipse Ti-E), equipped with 60x/1.4 NA objective and condenser lens of matching NA, 546/12 nm interference filter, liquid crystal device, polarization components, and processing software as described and available from OpenPolScope.org.

To perform temperature-dependent FUS studies by fluorescence microscopy, mixtures of 2 μM MBP-FUS wt (MBP-FUS(1–452), or MBP-FUS(ΔRRM)), 20 nM FUS-GFP (gift from Avinash Patel and Tony Hyman) and Tev protease were loaded onto a CherryTemp™ heater/cooler stage (Cherry BioTech). The FUS mixtures were treated with Tev protease at room temperature for 50 min to form phase-separated FUS droplets. The phase separated mixtures were cooled using the CherryTemp™ temperature controller to either 10°C or 15°C, held at those temperatures for 2 min, and then increased by 2°C increments to a maximum temperature of 43°C or 44°C. The sample was held at each temperature for 2–3 min prior to acquisition of a 50 μm Z-stack (1 μm increments) using spinning disk confocal microscopy. Maximum projection images from the Z-stack 10–50 μm above the slide surface were generated. To calculate T_{cloud}, images in this same portion of the Z-stack were segmented using the Triangle algorithm in ImageJ and the total number of FUS droplets was determined after a filter for circularity (>0.5) and size (>0.5 μm^2). T_{cloud} was determined from the x-intercept of a line fit to the first six (wt and FUS(1–452)) or eight (FUS(ΔRRM)) points in the (number of puncta) *vs.* temperature curve.

Dynamic light scattering analysis

Dynamic light scattering (DLS) was performed to examine polydispersity of MBP-FUS alone and the MBP-FUS•Kapβ2 complex. We used a DynPro DLS instrument (Wyatt Technology). Samples of 12 μM MBP-FUS ± 12 μM Kapβ2 in buffer containing 10 mM HEPES pH7.4, 150 mM NaCl, 10% glycerol and 2 mM 2-mercaptoethanol were loaded into the cuvette. Scattered light intensity at 25°C was analyzed using the software SEDPHAT.

To investigate whether Kapβ2 has attractive or repulsive self-interactions, we determined its diffusion coefficient at different protein concentrations, also using DLS. Prior to the experiment, Kapβ2 (in buffer containing 150 mM NaCl, 20 mM HEPES pH 7.5, 2 mM $Mg(OAc)_2$, 2 mM DTT, 10% glycerol) was centrifuged at 16,000 × g for 10 min and filtered through an ultrafree-MC GV centrifugal filter with a 0.22 μm pore size (EMD Millipore). Measurements were performed at 25 degree on a DynaPro DLS instrument (Wyatt Technology). The scattering intensities were averaged over twenty runs, each with a 20-second acquisition time. The diffusion coefficients were analyzed using Dynamics software (Wyatt Technology). Molecules with attractive interactions form larger species that diffuse more slowly as concentration increases; conversely, molecules with repulsive interactions do not self-associate, and diffuse more rapidly at higher concentrations interactions. The concentration dependence of diffusion coefficient (D) can be described approximately by $D = D_0(1+\kappa_D c)$, where D_0 is the diffusion coefficient at infinite dilution, c is the protein concentration and κ_D is the diffusion interaction parameter. A positive κ_D suggests net repulsive interactions and a negative κ_D indicates net attractive interactions (Connolly et al., 2012).

NMR analysis of FUS LC with Kapβ2

^{15}N-FUS LC (residues 1–163) was expressed by growing *E. coli* BL21 Star (DE3) in M9 minimal medium with $^{15}NH_4Cl$. ^{15}N-FUS LC was purified from inclusion bodies by resolubilizing in buffer containing 8M urea followed by HisTrap affinity chromatography and cleavage with TEV protease. The eluted protein was exchanged and concentrated into 20 mM CAPS pH 11.0 (no denaturant). To make samples for NMR, concentrated FUS LC was diluted into 20 mM MES/Bis-Tris (pH 6.6), 150 mM NaCl, 2 mM DTT, 10% glycerol and 0.01% NaN_3, followed by addition of 10% v/v D_2O. Samples with FUS LC and Kapβ2 variants were made identically, with Kapβ2 present in the MES/Bis-Tris buffer before addition of FUS LC. Independent samples were made for each Kapβ2 concentration.

NMR data for ^{15}N-labeled FUS LC were acquired at 10°C and 25°C on a Bruker 850 MHz spectrometer equipped with 5 mm cryogenically cooled triple- resonance pulsed field gradient (TCI) probe. Two-dimensional (2D) ^{1}H-^{15}N HSQC spectra were collected with spectral widths of 8928.6 Hz and 1723.5 Hz with 1536 and 256 complex data pairs in the ^{1}H and ^{15}N dimensions, respectively. An inter-scan delay of 1s was employed between successive transients. States-TPPI was employed for frequency discrimination in the indirectly detected dimension. Reference HSQC spectrum (without Kapβ2) was acquired on ^{15}N-labeled FUS LC (75 μM). To probe interactions between FUS LC and Kapβ2 or Kapβ2-FUS PY-NLS, 100 μM of unlabeled Kapβ2 or Kapβ2 bound to FUS PY-NLS (purified by size exclusion in presence of excess FUS PY-NLS and then exchanged by centrifugal filtration into NMR buffer) was added to the ^{15}N-labeled FUS LC in the stated ratios. Importantly, titrations were performed by generating a series of independent matched samples. All spectra were recorded in 5 mm NMR tubes and sample volume was always maintained to 500 μl in 90%H_2O/10%D_2O.

NMR analysis of FUS(164–526), FUS(164–500) and smaller FUS fragments with Kapβ2

Preparation of ^{15}N-labeled FUS(164–526), FUS(164–500) and RGG2-ZnF—^{15}N-labeled His_6-MBP-FUS(164–526), MBP-FUS(164–500) and MBP-RGG2-ZnF (FUS residues 371–452) were expressed by growing BL21(DE3) cells harboring the respective plasmids in M9 minimal medium (Muchmore et al., 1989) with $^{15}NH_4Cl$ as a sole source of nitrogen. Protein expression was induced with 1 mM IPTG, at 16 °C for 18 hours. Harvested cells were lyzed in buffer containing 20 mM Na-Phosphate buffer (pH 6.5), 1.5 M NaCl, 1 mM PMSF, 5 mM 2-mercaptoethanol (BME), 1μg/ml Leupeptin, 1 mM Benzamidine 1 μg/ml Antipain, and 10% Glycerol using EmulsiFlex-C5 (Avestin, Ottawa, Canada). ^{15}N-MBP-FUS(164–500) was purified by affinity chromatography using Amylose beads (washed extensively, first with buffer containing 20 mM Na-Phosphate pH 6.5, 1.5 M NaCl, 5 mM BME and then with the same buffer containing 1 M NaCl). On-bead TEV reaction was performed to remove MBP tag, and cleaved ^{15}N-FUS(164–500) was collected as flow-through and was dialyzed against buffer containing 20 mM HEPES (pH 7.4), 150 mM NaCl, 2 mM BME. The protein was further purified by cation exchange chromatography (Source 15S, GE healthcare life sciences). Fractions of clean FUS(164–500) were pooled and concentrated to 10 ml. NaCl concentration in the FUS(164–500) solution was then raised to 1M followed by gel filtration chromatography (Superdex 200 HiLoad 26/600) in buffer containing 20 mM HEPES (pH 7.4), 1 M NaCl, 2 mM BME. ^{15}N-labeled FUS(164–500)

elutes as a peak corresponding to monomeric molecular weight. Finally, ^{15}N-labeled FUS(164–500) was dialyzed against NMR buffer containing 20 mM Bis-Tris/MES (pH 6.5), 150 mM NaCl, 2 mM DTT, 10% glycerol, 1 mM NaN3. ^{15}N-MBP-RGG2-ZnF was purified similarly, except the gel filtration step was omitted. ^{15}N-FUS(164–526) was purified as ^{15}N-FUS(164–500) except the former was purified using Ni-NTA instead of amylose affinity chromatography.

Preparation of ^{2}H/15N/^{12}C-labeled FUS(164–500)—Deuterated ^{15}N-labeled MBP-FUS(164–500) was expressed by growing BL21(DE3) cells harboring plasmids for MBP-FUS(164–500) in modified M9+ medium (Cai et al 2016) in 100 % D_2O (99% $^{2}H_2O$, Cambridge isotope limited, inc) with $^{15}NH_4Cl$ and ^{12}C glucose-d6 (Cambridge isotope limited, inc) as sole source of nitrogen and carbon, respectively. The starter culture was prepared by inoculating 1 ml of LB with a single colony of freshly transformed BL21 cells. Cells were allowed to grow at 37 °C till OD_{600} reached 0.8 (~3 hrs). 400 µl of the previous culture was used to inoculate 10 ml of LB prepared in 100 % D_2O and subsequently 10 ml of LB/D_2O (OD_{600} 0.8) culture was used to inoculate 100 ml of medium M9+ medium. Cells were grown at 37 °C until OD_{600} reached ~4, and the whole culture was used to inoculate 1000 ml of M9+/D_2O and grown at 37 °C until OD_{600} reached 3.0. Protein expression was then induced with 0.8 mM IPTG, at 25°C for 30 hours. Harvested cells were lyzed and the protein purified as described for ^{15}N-labeled FUS(164–500) preparation except that final NMR buffer was 20 mM phosphate buffer (pH 6.5), 150 mM NaCl 2mM DTT, 10% glycerol and 1 mM NaN_3.

Preparation of ^{15}N-labeled RGG1, RGG1-RRM, RRM, ZnF and ZnF-RGG3—^{15}N-labeled His_6-MBP-RGG1 (FUS residues 164–267), His_6-MBP-RGG1-RRM (FUS residues 164–370), His_6-MBP-RRM (FUS residues 285–371), His_6-MBP-ZnF (FUS residues 415–460) and His_6-MBP-ZnF-RGG3 (FUS residues 421–500) proteins were expressed using the same protocol as protonated ^{15}N-labeled MBP-FUS(164–500). Cells were lysed in buffer containing 50 mM Tris pH 8.0, 10 mM Imidazole pH 7.5, 5 mM BME, 1 M NaCl, 1mM PMSF, 10% Glycerol, 1µg/ml Leupeptin, 1 mM Benzamidine, 1µg/ml Antipain. ^{15}N-labeled His_6-MBP-RGG1 and His_6-MBP-ZnF-RGG3 proteins were first purified on Ni-NTA beads (washed extensively buffer containing 50 mM Tris pH 8.0, 10 mM Imidazole pH7.5, 1 mM BME, 1.5 M NaCl, followed by second wash with buffer containing 50 mM TRIS pH 8.0, 25 mM Imidazole pH 7.5, 1 mM BME and 200 mM NaCl). Bound material was eluted with buffer containing 50 mM Tris pH 8.0, 500 mM Imidazole pH 7.5) 1 mM BME, 200 mM NaCl, and TEV was added to eluted materials for cleavage at 4 °C. Cleaved ^{15}N-labeled FUS fragments were further purified by cation exchange chromatography (Source 15S, GE healthcare life sciences), and pure proteins were then dialyzed against NMR buffer 20 mM Bis-Tris/MES pH 6.5, 150 mM NaCl, 2 mM DTT, 10% glycerol and 1 mM NaN3. ^{15}N-labeled RGG1-RRM was purified similarly except an additional final gel filtration (SD 75) step. His_6-MBP-RRM and His_6-MBP-ZnF were purified similarly except gel filtration (SD 75 or SD peptide 10/300, respectively) was substituted for cation exchange chromatography.

Cross saturation transfer experiment—In order to identify the interfaces between FUS(164–500) and Kapβ2•M9M, cross-saturation experiment (Takahashi et al., 2000) was

performed on an Agilent 800 MHz spectrometer equipped with a 5 mm cryogenically cooled triple-resonance pulsed field gradient (TRPFG) probe. Perdeuterated $^{2}H/^{15}N$-labeled FUS(164–500) (28 μM) was mixed with 42 μM of unlabeled Kapβ2•M9M in 90% H_2O/D_2O. Cross saturation of $^{2}H/^{15}N$ FUS was achieved by saturating aliphatic protons of Kapβ2•M9M for 1.5 s. A train of CHIRP adiabatic pulses with RF amplitude of 125 Hz, excitation centered at 2 ppm, which provided a 2400 Hz irradiation bandwidth, was used for saturation, followed by acquisition of ^{1}H-^{15}N TROSY (Pervushin et al., 1997) HSQC with an intertransient delay 2 s. A reference spectrum was acquired with the same experimental setup, except that center of CHIRP pulse train was shifted to ~50000 Hz off resonance (no saturation). Intensity of cross-peaks in irridiated (I, with saturation) and reference (I_0, no saturation) spectra were calculated by using nmrPipe (Delaglio et al., 1995) and Analysis module in CCPN (Vranken et al., 2005).

Line broadening experiments—NMR data for ^{15}N-labeled FUS(164–500) were acquired at 25°C on an Agilent 600 MHz spectrometer equipped with a 5 mm cryogenically cooled triple- resonance pulsed field gradient (TRPFG) probe. The sample temperature was maintained at 25 °C during all experiments. Two-dimensional (2D) ^{1}H-^{15}N HSQC spectra were collected with spectral widths of 8000 Hz and 1920 Hz and acquisition times of 64 ms and 67 ms in the ^{1}H and ^{15}N dimensions, respectively. An inter-scan delay of 1s was employed between successive transients. Rance-Kay mode of quadrature detection was employed for frequency discrimination in the indirectly detected dimension. Reference HSQC spectrum (without Kapβ2•FUS PY-NLS or Kapβ2•M9M) was acquired for 17 μM ^{15}N-labeled FUS(164–500). To probe interactions between FUS(164–500) and Kapβ2, 17 μM ^{15}N-FUS(164–500) was titrated with varying concentrations of unlabeled Kapβ2•FUS PY-NYLS (FUS(164–500):Kapβ2•FUS PY-NLS in molar ratios of 1:0.5, 1:1 and 1:2) and with unlabeled Kapβ2•M9M (FUS(164–500):Kapβ2•M9M molar ratio of 1:3). All spectra were recorded in a 5 mm NMR tubes and samples always maintained to 300 μl in 90%H_2O/10%D_2O. Each titration experiment was performed on a freshly prepared sample to avoid a dilution effect upon addition of the Kapβ2 complex.

NMR data for ^{15}N-FUS(164–526) were acquired similarly. To probe the interaction between FUS(164–526) and Kapβ2, ^{1}H-^{15}N spectra of 15 μM ^{15}N-FUS(164–526) were acquired in presence of 15 μM Kapβ2. A reference spectrum was acquired with 15 μM ^{15}N FUS (164–526) alone.

Interaction between FUS fragments and Kapβ2•M9M—In order to probe interaction between FUS fragments (RGG1, RGG1-RRM, RGG2-ZnF, ZnF-RGG3) and Kapβ2•M9M, different fragments (50 μM of each fragment) were titrated with Kapβ2•M9M (100 μM) in a 5 mm shigemi NMR tube. 2D ^{1}H-^{15}N HSQC spectra were acquired on an Agilent 600 MHz spectrometer equipped with a 5 mm cryogenically cooled triple- resonance pulsed field gradient (TRPFG) probe. All data were acquired at 25 °C in 90% H_2O/10% D_2O. Spectra were collected with sweep widths 8000 Hz and 1920 Hz and acquisition times of 64 ms and 67 ms in the ^{1}H and ^{15}N dimensions, respectively. An inter-transient delay of 1s was employed between successive transients. Rance-Kay mode of quadrature detection was employed for frequency discrimination in the indirectly detected dimension. A reference

experiment was acquired for each fragment (at 50 uM concentration) without Kapβ2•M9M, with the same experimental setup. Cross-peak intensities in absence (I_0) and presence (I) of Kapβ2•M9M were measured by using nmrPipe and Analysis module in CCPN.

All NMR data were processed using NMRPipe/NMRDraw processing software. Directly and indirectly detected time domain data were processed by applying a 90° phase-shifted squared sine bell or sine bell, respectively. Zero-filling was employed prior to Fourier transformation. Processed data were analyzed using the ipap.com script distributed with nmrPipe. The intensity of a resonance in the control experiment was taken as the reference intensity (I_0). The decrease in intensity (I) due to the line broadening and/or chemical exchange contribution to the relaxation, arising from interaction between ^{15}N-labeled FUS and Kapβ2 complex was determined by measuring peak volume/height. A ratio of I/I_0 as a function of residue number/peak number was plotted to assess the interacting residues on FUS.

Homology modeling was used to construct a model of the FUS zinc finger. A sequence similarity search of FUS zinc finger against sequences in the PDB performed on using BLAST (https://blast.ncbi.nlm.nih.gov/Blast.cgi?PAGE=Proteins) identified PDBID **2K1P** as the closest homolog (50% sequence identity). The homology model of the FUS zinc finger was built using SWISS-MODEL(Guex et al., 2009).

Small-angle X-ray scattering (SAXS)

SAXS experiments of MBP, MBP-FUS, Kapβ2, Kapβ2•FUS, and Kapβ2•MBP-FUS were carried out at Beamline 4–2 of the Stanford Synchrotron Radiation Lightsource (SSRL) in the SLAC National Accelerator Laboratory. At SSRL, the beam energy and current were 11 keV and 500 mA, respectively. A silver behenate sample was used to calibrate the q-range and detector distance. Data collection was controlled with Blu-Ice (Kim et al., 2014). We used an automatic sample delivery system equipped with a 1.5 mm-diameter thin-wall quartz capillary within which a sample aliquot was oscillated in the X-ray beam to minimize radiation damage (Kim et al., 2014). The sample was placed at 1.7 m from a MX225-HE (Rayonix, USA) CCD detector with a binned pixel size of 292 by 292 μm.

The SAXS profiles were collected at concentrations ranging from 0.5 either to 19.2 (Kapβ2) or up to 5.0 (all others) mg/mL. All protein samples were expressed and purified (as described above in Methods) in the protein storage buffers (10 mM HEPES pH 7.4, 150 mM NaCl, 20% glycerol, 2 mM $Mg(OAc)_2$, and 2 mM DTT for Kapβ2, 10 mM HEPES pH 7.4, 150 mM NaCl, 20% glycerol, 2 mM DTT, and protease inhibitors for Kapβ2-FUS, and 50 mM HEPES pH 7.4, 500 mM NaCl, 20% glycerol, 2 mM DTT, and protease inhibitors for all others). The 20% glycerol in the protein storage buffer protects the protein samples from radiation damage during X-ray exposure (Kim et al., 2014). To assess the potential effects of high glycerol concentration on the solution behavior of the proteins, we also collected SAXS profiles for all samples in buffer with 5% glycerol. No significant change in behavior was observed (Figure S7G); thus glycerol does not affect protein compaction in its low concentration ranging 5 to 20%. All solutions were filtered through 0.1 μm membranes (Millipore) to remove any aggregates. Up to 20 one-second exposures were used for each sample and buffer maintained at 15°C. Each of the resulting diffraction images was scaled

using the transmitted beam intensity, azimuthally integrated by SASTool (http://ssrl.slac.stanford.edu/~saxs/analysis/sastool.htm) and averaged to obtain fully processed data in the form of intensity versus q [$q=4\pi\sin(\theta)/\lambda$, θ=one-half of the scattering angle; λ=X-ray wavelength]. The buffer SAXS profile was subtracted from a protein SAXS profile. Subsequently, the mean of the lower concentration (0.5 – 1.0 mg/mL) profiles in the smaller scattering angle region ($q < 0.15$ Å^{-1}) and the mean of the higher concentration (1.5 – 5.0 or higher mg/mL) profiles in the wider scattering angle region ($q > 0.12$ Å^{-1}) were merged to obtain the final experimental SAXS profiles that are free of the concentration-dependent aggregation or polydispersity effect (Kikhney and Svergun, 2015).

The merged SAXS profiles were initially analyzed using the ATSAS package (Franke et al., 2017) to calculate radius of gyration (R_g^{SAXS}), maximum particle size (D_{max}), and pair distribution function (P(r)) (Figure 6E, Figure S6, and Table S4). The molecular weight (MW_{SAXS}) of each SAXS sample was estimated using SAXS MOW (Fischer et al., 2010) with a threshold of $q_{max} = 0.2 – 0.3$ Å^{-1} (Table S4). The *ab initio* shape of the corresponding protein (Figure S7; transparent envelope) was computed from the experimental SAXS profile by running DAMMIF 20 times, and then refined through additional 50 DAMMIN runs followed by superposition and averaging with DAMAVER (Franke et al., 2017).

X-ray crystallography of Kapβ2•FUS complexes

To assemble and purify Kapβ2•FUS complexes for crystallization, bacteria expressing GST-Kapβ2Δloop and MBP-FUS were mixed and lysed together. Kapβ2•FUS complex was purified by tandem affinity chromatography using GSH sepharose beads and amylose resin, cleaved with TEV protease, and purified by gel filtration chromatography in buffer containing 20 mM HEPES, pH 7.4, 110 mM potassium acetate, 2 mM DTT, 2 mM magnesium acetate, 1 mM EGTA and 20% glycerol. Kapβ2•FUS complexes were concentrated to 10 mg/mL for crystallization.

All Kapβ2•FUS crystals were obtained by hanging drop vapor diffusion at 20°C (1.0 μL protein + 1.0 μL reservoir solution) with reservoir solution of 0.8 M Succinic acid pH 7.0. Crystals were cryo-protected by addition of ~25% glycerol, and flash-cooled by immersion in liquid nitrogen. 0.9795Å wavelength X-ray diffraction data were collected at the Advance Photon Source 19ID beamline in the Structural Biology Center at Argonne National Laboratory. Diffraction data was indexed, integrated, and scaled using HKL3000 (Minor et al., 2006). The structure was determined by molecular replacement using PHASER with a search model of human Kapβ2 (Chain A from PDB ID 4FDD) (Cansizoglu and Chook, 2007). Several rounds of refinement using PHENIX and manual model building with Coot were performed (Adams et al., 2010; Emsley et al., 2010). X-triage analysis of the dataset for KapB2•full-length FUS indicated pseudo-merohedral twinning (Adams et al., 2010). Therefore the data was refined in phenix.refine with twin law I,-k,h, and twin fraction was refined to 36% (Afonine et al., 2012). FUS residues were built into the electron density maps at the last stages of the refinement. Final models of Kapβ2•FUS complexes show excellent stereochemical parameters based on Molprobity suite in PHENIX (Chen et al., 2010). Illustrations were prepared with PyMOL (Schrodinger, 2015). Kicked OMIT maps are calculated with PHENIX by omitting FUS.

Quantification and Statistical Analysis

Turbidity analyses in Figures 1B–D, 2A–C, 5A–C and Supplemental Figure S1E were each repeated three times. Standard deviation error bars were obtained from three technical replicates.

X-ray diffraction data was indexed, integrated and scaled using software HKL3000. Completeness, R_{merge}, $I/\sigma I$ and CC1/2 values were used to evaluate data. R_{work} and R_{free} were used to evaluate PHENIX-refined models, which were validated using the Molprobity suite in PHENIX.

ITC data in Figures S1B, S2B and S2C, collected in triplicates using the MicroCal iTC_{200} software. Individual thermograms were integrated and processed into binding isotherms using the NITPIC software. Analysis by NITPIC produces error of each titration, the incompentency of Kapβ2 and the binding isotherms. Triplicate isotherms are then populated into the SEDPHAT software for global fitting. A rigorous statistical analysis of the best fit is carried out using F-statistics. The triplicate datasets are then presented using GUSSI.

NMR analysis—Error in resonance intensity measurements reported in Figures 3, 4, 5, S3 and S5 were calculated by measuring signal-to-nosie ratio.

Data and Software Availability

The crystal structures of Kapβ2•FUS(full-length), Kapβ2•FUS(371–526) and Kapβ2•FUS(456–526) have been deposited in the Protein Data Bank under codes **5YVG**, **5YVH** and **5YVI**.

Supplementary Material

Refer to Web version on PubMed Central for supplementary material.

Acknowledgments

We thank D. Dormann and J. Shorter for critical reading of the manuscript. We thank A. Patel and A. A. Hyman for their gift of FUS-GFP, T. Cagatay and A. Gonzalez for help subcloning, J. Hu and D. Corey for their help with temperature-dependent turbidity analysis, N. Conrad and K. Lynch for advice on FUS-RNA analysis, T. Matsui and T.M. Weiss at SSRL, SLAC National Accelerator Laboratory, for assistance with collecting SAXS data, and B. Raveh for discussions on SAXS analysis. We thank D. Tomchick for advice on X-ray structure determination, and the Structural Biology Laboratory and Macromolecular Biophysics Resource at UTSW for their assistance with crystallographic and biophysical data collection. Crystallographic results are derived from work performed at Argonne National Laboratory, Structural Biology Center at the Advanced Photon Source. Argonne is operated by UChicago Argonne, LLC, for the U.S. Department of Energy (DOE), Office of Biological and Environmental Research (BER) under contract DE-AC02-06CH11357. NMR data were obtained in part at the Brown University Structural Biology Core Facility supported by the Division of Biology and Medicine, Brown University. NMR spectroscopy at UTSW is supported by NIH instrumentation grants 1S10RR26461-1 and 1S10OD018027-01. SAXS experiments were performed at the SSRL, SLAC National Accelerator Laboratory operated for DOE by Stanford University. The SSRL SMBP is supported by the DOE BER, by the National Institutes of Health (NIH), NCRR, Biomedical Technology Program (P41RR001209), and by NIGMS, NIH (P41GM103393). This work was funded by NIGMS of NIH under Awards R01GM069909 (Y.M.C.), U01GM98256-01 (Y.M.C and A.S.), R01GM56322 (M.K.R.), R01GM118530 (N.L.F), R01GM083960 (A.S), P41GM109824 (A.S), R01GM112108 (A.S), and R01GM114274 (R.O.), T32GM008203 (J.J.), T32GM008297 (J.M.B.), the Howard Hughes Medical Institute HCIA grant (M.K.R.), the Welch Foundation Grants I-1532 (Y.M.C.) and I-1544 (M.K.R.), Leukemia and Lymphoma Society Scholar Award (Y.M.C.), the University of Texas Southwestern Endowed Scholars Program (Y.M.C.). Work in M.K.R's lab was supported by the Howard Hughes Medical Institute. R.A. was an American

Heart Association Postdoctoral Fellow and H.Y.J.F was a Howard Hughes Medical Institute International Student Research fellow.

References

Adams PD, Afonine PV, Bunkoczi G, Chen VB, Davis IW, Echols N, Headd JJ, Hung LW, Kapral GJ, Grosse-Kunstleve RW, et al. PHENIX: a comprehensive Python-based system for macromolecular structure solution. Acta Crystallogr D Biol Crystallogr. 2010; 66:213–221. [PubMed: 20124702]

Afonine PV, Grosse-Kunstleve RW, Echols N, Headd JJ, Moriarty NW, Mustyakimov M, Terwilliger TC, Urzhumtsev A, Zwart PH, Adams PD. Towards automated crystallographic structure refinement with phenix.refine. Acta Crystallogr D Biol Crystallogr. 2012; 68:352–367. [PubMed: 22505256]

Banani SF, Lee HO, Hyman AA, Rosen MK. Biomolecular condensates: organizers of cellular biochemistry. Nat Rev Mol Cell Biol. 2017

Brangwynne CP, Tompa P, Pappu RV. Polymer physics of intracellular phase transitions. Nat Phys. 2015; 11:899–904.

Brautigam CA. Calculations and Publication-Quality Illustrations for Analytical Ultracentrifugation Data. Methods Enzymol. 2015; 562:109–133. [PubMed: 26412649]

Brautigam CA, Zhao H, Vargas C, Keller S, Schuck P. Integration and global analysis of isothermal titration calorimetry data for studying macromolecular interactions. Nat Protoc. 2016; 11:882–894. [PubMed: 27055097]

Burke KA, Janke AM, Rhine CL, Fawzi NL. Residue-by-Residue View of In Vitro FUS Granules that Bind the C-Terminal Domain of RNA Polymerase II. Mol Cell. 2015; 60:231–241. [PubMed: 26455390]

Cansizoglu AE, Chook YM. Conformational heterogeneity of karyopherin beta2 is segmental. Structure. 2007; 15:1431–1441. [PubMed: 17997969]

Cansizoglu AE, Lee BJ, Zhang ZC, Fontoura BM, Chook YM. Structure-based design of a pathway-specific nuclear import inhibitor. Nat Struct Mol Biol. 2007; 14:452–454. [PubMed: 17435768]

Chen VB, Arendall WB 3rd, Headd JJ, Keedy DA, Immormino RM, Kapral GJ, Murray LW, Richardson JS, Richardson DC. MolProbity: all-atom structure validation for macromolecular crystallography. Acta crystallographica Section D, Biological crystallography. 2010; 66:12–21. [PubMed: 20057044]

Chook YM, Blobel G. Structure of the nuclear transport complex karyopherin-beta2-Ran x GppNHp. Nature. 1999; 399:230–237. [PubMed: 10353245]

Chook YM, Jung A, Rosen MK, Blobel G. Uncoupling Kapbeta2 substrate dissociation and ran binding. Biochemistry. 2002; 41:6955–6966. [PubMed: 12033928]

Chook YM, Suel KE. Nuclear import by karyopherin-betas: recognition and inhibition. Biochim Biophys Acta. 2011; 1813:1593–1606. [PubMed: 21029754]

Connolly BD, Petry C, Yadav S, Demeule B, Ciaccio N, Moore JM, Shire SJ, Gokarn YR. Weak interactions govern the viscosity of concentrated antibody solutions: high-throughput analysis using the diffusion interaction parameter. Biophys J. 2012; 103:69–78. [PubMed: 22828333]

Conti E, Izaurralde E. Nucleocytoplasmic transport enters the atomic age. Curr Opin Cell Biol. 2001; 13:310–319. [PubMed: 11343901]

Crozat A, Aman P, Mandahl N, Ron D. Fusion of CHOP to a novel RNA-binding protein in human myxoid liposarcoma. Nature. 1993; 363:640–644. [PubMed: 8510758]

Dong X, Biswas A, Suel KE, Jackson LK, Martinez R, Gu H, Chook YM. Structural basis for leucine-rich nuclear export signal recognition by CRM1. Nature. 2009; 458:1136–1141. [PubMed: 19339969]

Dormann D, Haass C. TDP-43 and FUS: a nuclear affair. Trends Neurosci. 2011; 34:339–348. [PubMed: 21700347]

Dormann D, Rodde R, Edbauer D, Bentmann E, Fischer I, Hruscha A, Than ME, Mackenzie IR, Capell A, Schmid B, et al. ALS-associated fused in sarcoma (FUS) mutations disrupt Transportin-mediated nuclear import. Embo J. 2010; 29:2841–2857. [PubMed: 20606625]

Ederle H, Dormann D. TDP-43 and FUS en route from the nucleus to the cytoplasm. FEBS Lett. 2017; 591:1489–1507. [PubMed: 28380257]

Emsley P, Lohkamp B, Scott WG, Cowtan K. Features and development of Coot. Acta crystallographica Section D, Biological crystallography. 2010; 66:486–501. [PubMed: 20383002]

Erickson HP. Size and Shape of Protein Molecules at the Nanometer Level Determined by Sedimentation, Gel Filtration, and Electron Microscopy. Biol Proced Online. 2009; 11:32–51. [PubMed: 19495910]

Fischer H, Neto MD, Napolitano HB, Polikarpov I, Craievich AF. Determination of the molecular weight of proteins in solution from a single small-angle X-ray scattering measurement on a relative scale. J Appl Crystallogr. 2010; 43:101–109.

Franke D, Petoukhov MV, Konarev PV, Panjkovich A, Tuukkanen A, Mertens HDT, Kikhney AG, Hajizadeh NR, Franklin JM, Jeffries CM, et al. ATSAS 2.8: a comprehensive data analysis suite for small-angle scattering from macromolecular solutions. J Appl Crystallogr. 2017; 50:1212–1225. [PubMed: 28808438]

Fung HY, Chook YM. Atomic basis of CRM1-cargo recognition, release and inhibition. Semin Cancer Biol. 2014; 27:52–61. [PubMed: 24631835]

Fung HY, Fu SC, Brautigam CA, Chook YM. Structural determinants of nuclear export signal orientation in binding to exportin CRM1. Elife. 2015; 4

Guex N, Peitsch MC, Schwede T. Automated comparative protein structure modeling with SWISS-MODEL and Swiss-PdbViewer: A historical perspective. Electrophoresis. 2009; 30:S162–S173. [PubMed: 19517507]

Harrison AF, Shorter J. RNA-binding proteins with prion-like domains in health and disease. Biochem J. 2017; 474:1417–1438. [PubMed: 28389532]

Hough LE, Dutta K, Sparks S, Temel DB, Kamal A, Tetenbaum-Novatt J, Rout MP, Cowburn D. The molecular mechanism of nuclear transport revealed by atomic-scale measurements. Elife. 2015; 4

Iko Y, Kodama TS, Kasai N, Oyama T, Morita EH, Muto T, Okumura M, Fujii R, Takumi T, Tate S, et al. Domain Architectures and characterization of an RNA-binding protein, TLS. Journal of Biological Chemistry. 2004; 279:44834–44840. [PubMed: 15299008]

Jakel S, Mingot JM, Schwarzmaier P, Hartmann E, Gorlich D. Importins fulfil a dual function as nuclear import receptors and cytoplasmic chaperones for exposed basic domains. Embo Journal. 2002; 21:377–386. [PubMed: 11823430]

Jayalakshmi V, Krishna NR. Complete relaxation and conformational exchange matrix (CORCEMA) analysis of intermolecular saturation transfer effects in reversibly forming ligand-receptor complexes. J Magn Reson. 2002; 155:106–118. [PubMed: 11945039]

Ju S, Tardiff DF, Han H, Divya K, Zhong Q, Maquat LE, Bosco DA, Hayward LJ, Brown RH Jr, Lindquist S, et al. A yeast model of FUS/TLS-dependent cytotoxicity. PLoS Biol. 2011; 9:e1001052. [PubMed: 21541368]

Kato M, Han TW, Xie S, Shi K, Du X, Wu LC, Mirzaei H, Goldsmith EJ, Longgood J, Pei J, et al. Cell-free formation of RNA granules: low complexity sequence domains form dynamic fibers within hydrogels. Cell. 2012; 149:753–767. [PubMed: 22579281]

Kikhney AG, Svergun DI. A practical guide to small angle X-ray scattering (SAXS) of flexible and intrinsically disordered proteins. FEBS Lett. 2015; 589:2570–2577. [PubMed: 26320411]

Kim SJ, Fernandez-Martinez J, Sampathkumar P, Martel A, Matsui T, Tsuruta H, Weiss TM, Shi Y, Markina-Inarrairaegui A, Bonanno JB, et al. Integrative structure-function mapping of the nucleoporin Nup133 suggests a conserved mechanism for membrane anchoring of the nuclear pore complex. Mol Cell Proteomics. 2014; 13:2911–2926. [PubMed: 25139911]

King OD, Gitler AD, Shorter J. The tip of the iceberg: RNA-binding proteins with prion-like domains in neurodegenerative disease. Brain Res. 2012; 1462:61–80. [PubMed: 22445064]

Kobayashi J, Matsuura Y. Structural basis for cell-cycle-dependent nuclear import mediated by the karyopherin Kap121p. J Mol Biol. 2013; 425:1852–1868. [PubMed: 23541588]

Lee BJ, Cansizoglu AE, Suel KE, Louis TH, Zhang Z, Chook YM. Rules for nuclear localization sequence recognition by karyopherin beta 2. Cell. 2006; 126:543–558. [PubMed: 16901787]

Li YR, King OD, Shorter J, Gitler AD. Stress granules as crucibles of ALS pathogenesis. Journal of Cell Biology. 2013; 201:361–372. [PubMed: 23629963]

Lin Y, Currie SL, Rosen MK. Intrinsically disordered sequences enable modulation of protein phase separation through distributed tyrosine motifs. J Biol Chem. 2017

Lin Y, Protter DS, Rosen MK, Parker R. Formation and Maturation of Phase-Separated Liquid Droplets by RNA-Binding Proteins. Mol Cell. 2015; 60:208–219. [PubMed: 26412307]

Liu XH, Niu CY, Ren JT, Zhang JY, Xie XD, Zhu HN, Feng W, Gong WM. The RRM domain of human fused in sarcoma protein reveals a non-canonical nucleic acid binding site. Bba-Mol Basis Dis. 2013; 1832:375–385.

Loughlin FE, Mansfield RE, Vaz PM, McGrath AP, Setiyaputra S, Gamsjaeger R, Chen ES, Morris BJ, Guss JM, Mackay JP. The zinc fingers of the SR-like protein ZRANB2 are single-stranded RNA-binding domains that recognize 5′ splice site-like sequences. Proc Natl Acad Sci U S A. 2009; 106:5581–5586. [PubMed: 19304800]

Milles S, Mercadante D, Aramburu IV, Jensen MR, Banterle N, Koehler C, Tyagi S, Clarke J, Shammas SL, Blackledge M, et al. Plasticity of an ultrafast interaction between nucleoporins and nuclear transport receptors. Cell. 2015; 163:734–745. [PubMed: 26456112]

Minor W, Cymborowski M, Otwinowski Z, Chruszcz M. HKL-3000: the integration of data reduction and structure solution--from diffraction images to an initial model in minutes. Acta crystallographica Section D, Biological crystallography. 2006; 62:859–866. [PubMed: 16855301]

Mittag T, Orlicky S, Choy WY, Tang X, Lin H, Sicheri F, Kay LE, Tyers M, Forman-Kay JD. Dynamic equilibrium engagement of a polyvalent ligand with a single-site receptor. Proc Natl Acad Sci U S A. 2008; 105:17772–17777. [PubMed: 19008353]

Molliex A, Temirov J, Lee J, Coughlin M, Kanagaraj AP, Kim HJ, Mittag T, Taylor JP. Phase Separation by Low Complexity Domains Promotes Stress Granule Assembly and Drives Pathological Fibrillization. Cell. 2015; 163:123–133. [PubMed: 26406374]

Monahan Z, Ryan VH, Janke AM, Burke KA, Rhoads SN, Zerze GH, O'Meally R, Dignon GL, Conicella AE, Zheng W, et al. Phosphorylation of the FUS low-complexity domain disrupts phase separation, aggregation, and toxicity. EMBO J. 2017; 36:2951–2967. [PubMed: 28790177]

Murakami T, Qamar S, Lin JQ, Schierle GS, Rees E, Miyashita A, Costa AR, Dodd RB, Chan FT, Michel CH, et al. ALS/FTD Mutation-Induced Phase Transition of FUS Liquid Droplets and Reversible Hydrogels into Irreversible Hydrogels Impairs RNP Granule Function. Neuron. 2015; 88:678–690. [PubMed: 26526393]

Murray DT, Kato M, Lin Y, Thurber KR, Hung I, McKnight SL, Tycko R. Structure of FUS Protein Fibrils and Its Relevance to Self-Assembly and Phase Separation of Low-Complexity Domains. Cell. 2017; 171:615–627. e616. [PubMed: 28942918]

Ohshima T, Nakajima T, Oishi T, Imamoto N, Yoneda Y, Fukamizu A, Yagami K. CRM1 mediates nuclear export of nonstructural protein 2 from parvovirus minute virus of mice. Biochem Biophys Res Commun. 1999; 264:144–150. [PubMed: 10527855]

Oldenbourg R. Analysis of edge birefringence. Biophys J. 1991; 60:629–641. [PubMed: 1932552]

Oldenbourg R, Mei G. New polarized light microscope with precision universal compensator. J Microsc. 1995; 180:140–147. [PubMed: 8537959]

Ozdilek BA, Thompson VF, Ahmed NS, White CI, Batey RT, Schwartz JC. Intrinsically disordered RGG/RG domains mediate degenerate specificity in RNA binding. Nucleic Acids Res. 2017; 45:7984–7996. [PubMed: 28575444]

Patel A, Lee HO, Jawerth L, Maharana S, Jahnel M, Hein MY, Stoynov S, Mahamid J, Saha S, Franzmann TM, et al. A Liquid-to-Solid Phase Transition of the ALS Protein FUS Accelerated by Disease Mutation. Cell. 2015; 162:1066–1077. [PubMed: 26317470]

Port SA, Monecke T, Dickmanns A, Spillner C, Hofele R, Urlaub H, Ficner R, Kehlenbach RH. Structural and Functional Characterization of CRM1-Nup214 Interactions Reveals Multiple FG-Binding Sites Involved in Nuclear Export. Cell Rep. 2015; 13:690–702. [PubMed: 26489467]

Ryu HH, Jun MH, Min KJ, Jang DJ, Lee YS, Kim HK, Lee JA. Autophagy regulates amyotrophic lateral sclerosis-linked fused in sarcoma-positive stress granules in neurons. Neurobiol Aging. 2014; 35:2822–2831. [PubMed: 25216585]

Scheuermann TH, Brautigam CA. High-precision, automated integration of multiple isothermal titration calorimetric thermograms: new features of NITPIC. Methods. 2015; 76:87–98. [PubMed: 25524420]

Schrodinger, LLC. The PyMOL Molecular Graphics System, Version 1.8. 2015.

Schwartz JC, Cech TR, Parker RR. Biochemical Properties and Biological Functions of FET Proteins. Annu Rev Biochem. 2015; 84:355–379. [PubMed: 25494299]

Schwartz JC, Wang X, Podell ER, Cech TR. RNA seeds higher-order assembly of FUS protein. Cell Rep. 2013; 5:918–925. [PubMed: 24268778]

Soniat M, Chook YM. Karyopherin-beta2 Recognition of a PY-NLS Variant that Lacks the Proline-Tyrosine Motif. Structure. 2016; 24:1802–1809. [PubMed: 27618664]

Sun Z, Diaz Z, Fang X, Hart MP, Chesi A, Shorter J, Gitler AD. Molecular determinants and genetic modifiers of aggregation and toxicity for the ALS disease protein FUS/TLS. PLoS Biol. 2011; 9:e1000614. [PubMed: 21541367]

Takahama K, Oyoshi T. Specific binding of modified RGG domain in TLS/FUS to G-quadruplex RNA: tyrosines in RGG domain recognize 2′-OH of the riboses of loops in G-quadruplex. J Am Chem Soc. 2013; 135:18016–18019. [PubMed: 24251952]

Ueda T, Takeuchi K, Nishida N, Stampoulis P, Kofuku Y, Osawa M, Shimada I. Cross-saturation and transferred cross-saturation experiments. Q Rev Biophys. 2014; 47:143–187. [PubMed: 24780282]

Xiang SH, Kato M, Wu LC, Lin Y, Ding M, Zhang YJ, Yu YH, McKnight SL. The LC Domain of hnRNPA2 Adopts Similar Conformations in Hydrogel Polymers, Liquid-like Droplets, and Nuclei. Cell. 2015; 163:829–839. [PubMed: 26544936]

Zhang ZC, Chook YM. Structural and energetic basis of ALS-causing mutations in the atypical proline-tyrosine nuclear localization signal of the Fused in Sarcoma protein (FUS). Proc Natl Acad Sci U S A. 2012; 109:12017–12021. [PubMed: 22778397]

Zhao H, Piszczek G, Schuck P. SEDPHAT--a platform for global ITC analysis and global multi-method analysis of molecular interactions. Methods. 2015; 76:137–148. [PubMed: 25477226]

- Karyopherin-β2 inhibits liquid-liquid phase separation of FUS
- Kapβ2 binds tightly to the PY-NLS and weakly to multiple regions across FUS
- Many of these regions also promote FUS phase separation
- Kapβ2-FUS interactions compete with FUS-FUS interactions to disrupt phase separation

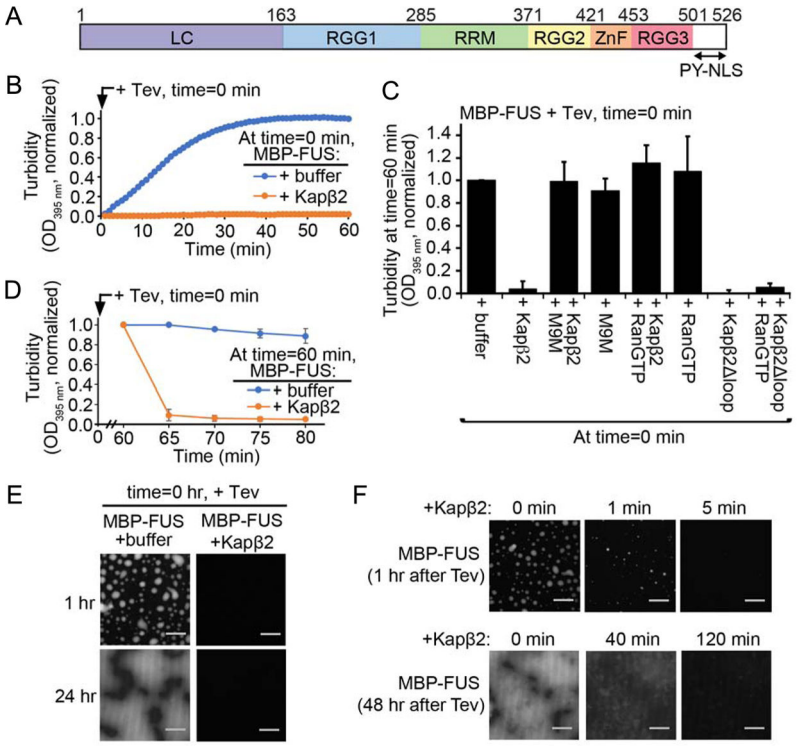

Figure 1. Kapβ2 inhibits FUS turbidity and phase separation in a PY-NLS- and RanGTP-dependent manner

A) Domain organization of FUS. **B**) Turbidity of 8 μM MBP-FUS ± 8 μM Kapβ2, measured for 60 min at room temperature after addition of Tev protease to remove MBP from MBP-FUS. **C**) Turbidity of 8 μM MBP-FUS in the presence of buffer, 8 μM Kapβ2 ± RanGTP or inhibitor M9M, or Kapβ2Δloop ± RanGTP (60 min after Tev). **D)** Either 8 μM Kapβ2 or buffer was added at time=60 min to turbid FUS (8 μM MBP-FUS pre-treated with Tev for 60 min) and OD_{395nm} measured for the next 20 min. **B**)-**D**), OD_{395nm} normalized to measurements of MBP-FU+buffer+Tev at time=60 min. **C)-D)**, mean of 3 technical replicates, ± S.D. **E**) Mixtures containing 5 μM MBP-FUS, 0.5 μM MBP-FUS-$SNAP^{SNAP\text{-}Surface\ 649}$ and either buffer or 10 μM Kapβ2 were treated with Tev and imaged 1 hr later. (Supplementary Movie 1 also shows FUS droplets at time=1 hr.) **F**) Mixtures of 5 μM MBP-FUS and 0.5 μM MBP-FUS-$SNAP^{SNAP\text{-}Surface\ 649}$ were treated with Tev for 1 hr prior to addition of 10 μM of Kapβ2, which cleared FUS droplets in less than 5 min (see also Supplementary Movie 2). Kapβ2 added to phase separated FUS 48 hr after Tev treatment cleared most of the phase separated material in 120 min (Supplementary Movie 3 also shows the first 30 min after Kapβ2 addition). Images in **E)-F)** were obtained with spinning disk confocal microscopy (561 nm laser illumination; 60x 1.4na oil immersion objective lenses) and 20 μm length scale bars are shown. See also Figure S1.

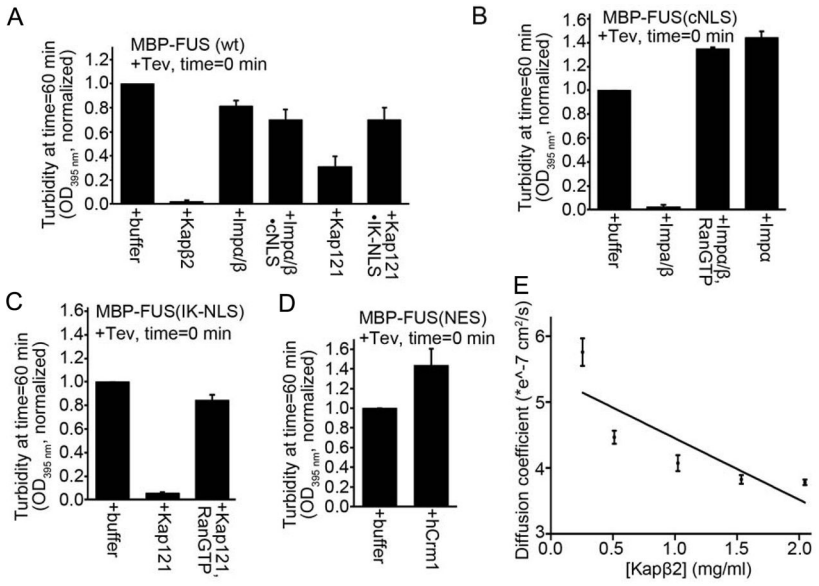

Figure 2. Imp-α/β and Kap121 inhibit FUS phase separation when their NLS is introduced into FUS, but Kapβ2 does not act non-specifically to inhibit FUS phase separation

A) Turbidity of wildtype FUS in the presence of buffer, Kapβ2, Impα/β, cNLS-bound Impα/β, Kap121 or IK-NLS-bound Kap121. **B)** Turbidity of FUS(cNLS) chimera (FUS PY-NLS replaced with the SV40 T antigen cNLS) in the presence of buffer, Impα/β, Impα/β•RanGTP or Impα. **C)** Turbidity of FUS(IK-NLS) chimera (PY-NLS replaced with IK-NLS from Pho4) in the presence of buffer, Kap121 or Kap121•RanGTP. **D)** Turbidity of FUS(NES) chimera (PY-NLS replaced with the NES from the NS2 protein of MVM virus) in the presence of buffer or CRM1. 8 μM proteins were used in **A)-D)**, and OD_{395nm} were normalized to those of MBP-FUS+buffer+Tev at time=60 min. **E)** Diffusion coefficients of Kapβ2 were measured at different concentrations by dynamic light scattering. Error bars represent S.D. from 3 technical replicates. See also Figure S2 and Table S1.

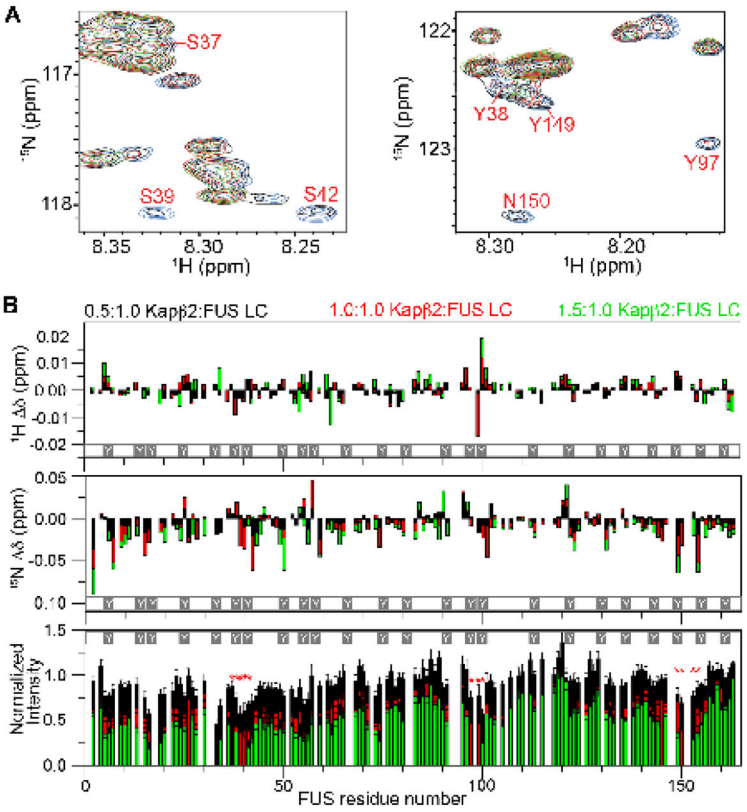

Figure 3. Kapβ2 interacts weakly and non-uniformly with residues in FUS LC

A) Overlay of 2D ^{1}H-^{15}N spectra of 75 μM ^{15}N-FUS LC alone (blue) or with increasing concentrations of Kapβ2: 37.5 μM (0.5:1, black), 75 μM (1:1, red), 112.5 μM (1.5:1, green), showing three of the FUS LC regions (residues 37–41, 97–100, 149–154) most affected by Kapβ2 resulting in chemical shifts and intensity attenuations. **B)** Titrations at 10 °C of 75 μM FUS LC with increasing concentrations of Kapβ2 compared to FUS LC alone. NMR chemical shift deviations, ^{1}H (top) and ^{15}N (middle), and resonance intensity attenuation (bottom) are plotted. Increasing extent of chemical shift differences of ^{1}H and ^{15}N resonance position, as well as resonance intensity attenuation, support Kapβ2 binding weakly to across the entire FUS LC domain. Resonance intensity attenuation and chemical shifts are non-uniformly distributed as segments ^{37}SYSGY^{41}, ^{97}YPGY^{100} and ^{149}YSPPSG^{154} (white Ys mark the 24 tyrosines in FUS LC) show the largest perturbations in amide resonance intensity (red asterisks, bottom panel) in the presence of Kapβ2. These segments also show large ^{15}N and/or ^{1}H chemical shift deviations. See also Figure S3.

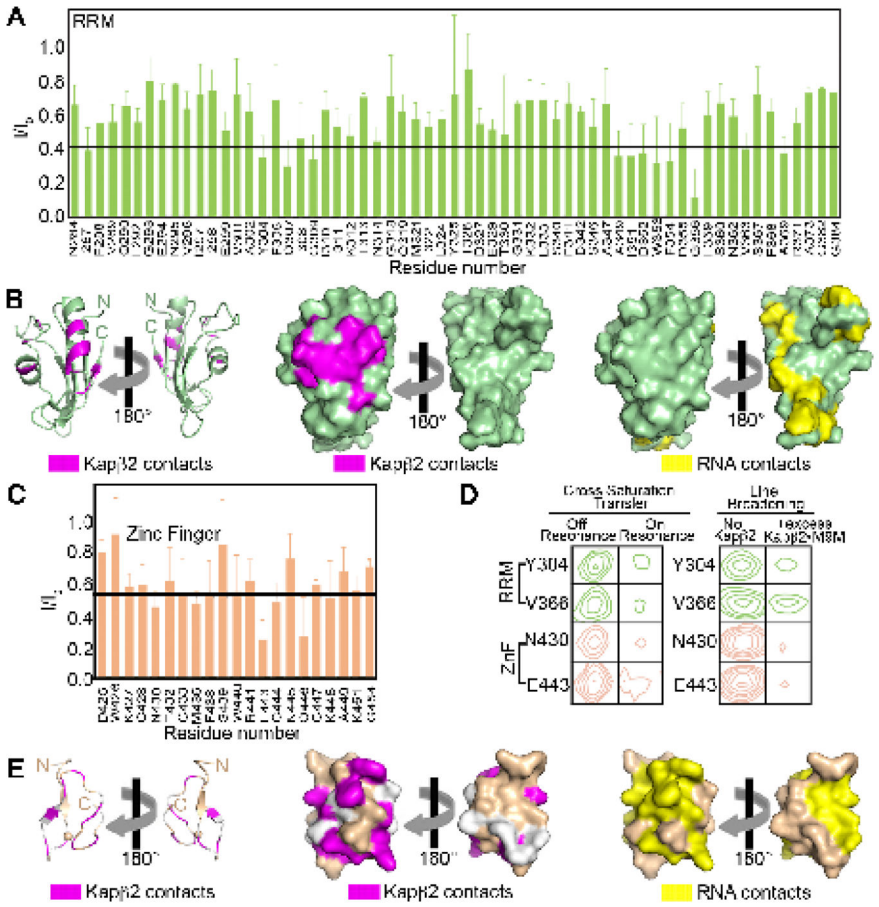

Figure 4. Kapβ2 interacts weakly with the folded RRM and ZnF domains within FUS(164–500)

A) Attenuations in intensity (I/I_0) of assigned RRM domain non-proline resonances in FUS(164–500) in the cross saturation transfer experiment. Deuterated ^{15}N-FUS(164–500) was cross saturated from protonated Kapβ2-M9M (1.5-fold molar excess) and intensities of assigned RRM resonances were measured with (I) and without (I_0) irradiation in aliphatic region. **B)** Ribbon (left) and surface (middle and right panels) representations of the RRM (PDBID **1LCW**; green), showing binding sites for Kapβ2 (magenta, residues with I/I_0<0.4 in cross saturation experiment) and RNA (yellow). **C)** Same as **(A)**, but shown here are I/I_0 of assigned ZnF domain non-proline resonances in FUS(164–500) in the cross saturation transfer experiment. **D)** Selected resonances of RRM (green) and ZnF (orange) domains from TROSY ^{1}H-^{15}N HSQC/^{1}H-^{15}N HSQC NMR spectra of ^{15}N-FUS(164–500) showing change in intensity in cross saturation and line broadening experiments upon addition of 3-fold molar excess Kapβ2-M9M. **E)** Homology model of the FUS ZnF domain (orange; from ZnF in ZNF265, PDBID **2K1P**). Ribbon (left) and surface (middle and right) representations showing binding sites for Kapβ2 (magenta, residues with I/I_0<0.55 in cross saturation experiment) and RNA (yellow). Residues with unassigned/missing/proline resonances are in white. See also Figure S4.

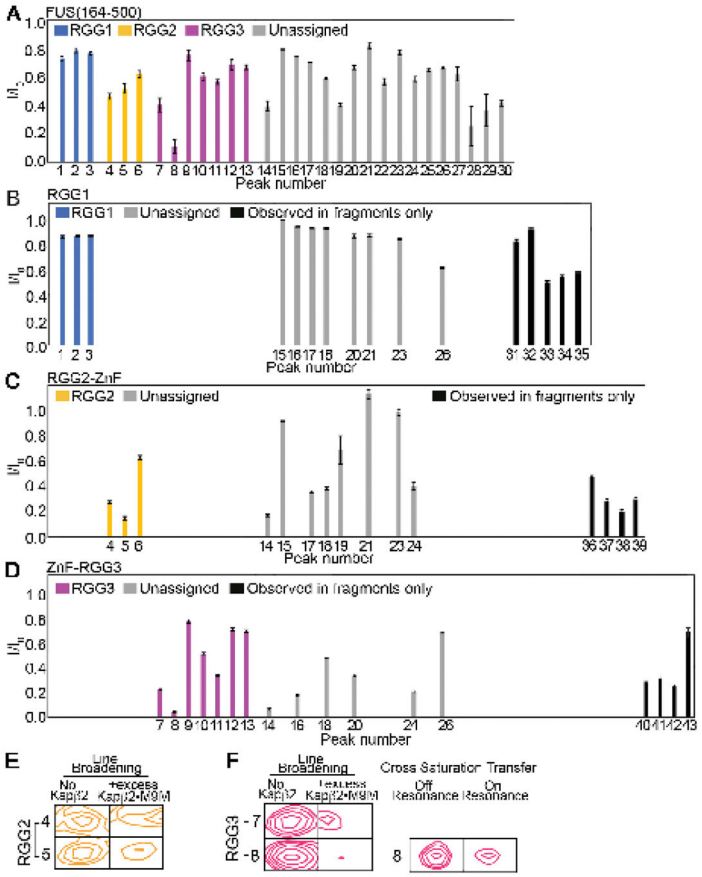

Figure 5. Kapβ2 interacts with disordered RGG regions

Attenuation of glycine resonances in $^{1}H/^{15}N$ HSQC NMR spectra of ^{15}N-FUS(164–500) **(A)**, RGG1 **(B)**, RGG2-ZnF **(C)** and ZnF-RGG3 **(D)** upon addition of 2-fold molar excess of Kapβ2•M9M. **E–F)** Selected glycine amide resonances of RGG2 **(E)** and RGG3 (**F**, left) in ^{1}H-^{15}N HSQC spectra ± 2-fold molar excess Kapβ2•M9M. **F)** Right, selected glycine amide resonances of RGG3 in ^{1}H-^{15}N TROSY-based cross saturation transfer experiments in the presence of a 1.5-fold molar excess of Kapβ2•M9M with off- or on-resonance saturation. Cross saturation experiment was performed on $^{2}H/^{15}N$-FUS(164–500) complexed with unlabeled Kapβ2•M9M in 1:1.5 molar ratio. See also Figure S5, Tables S2 and S3.

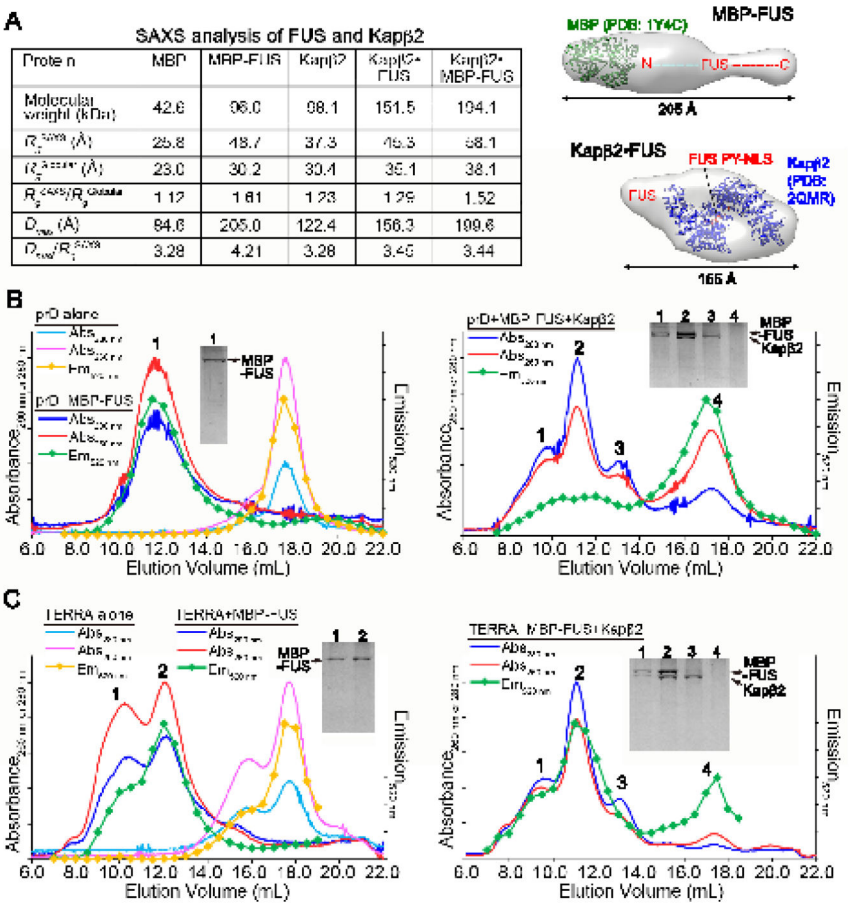

Protein	MBP	MBP-FUS	Kapβ2	Kapβ2•FUS	Kapβ2•MBP-FUS
Molecular weight (kDa)	42.6	96.0	98.1	151.5	194.1
R_g^{SAXS} (Å)	25.8	48.7	37.3	46.3	58.1
$R_g^{Globular}$ (Å)	23.0	30.2	30.4	35.1	38.1
$R_g^{SAXS}/R_g^{Globular}$	1.12	1.61	1.23	1.29	1.52
D_{max} (Å)	84.6	205.0	122.4	156.3	199.6
D_{max}/R_g^{SAXS}	3.28	4.21	3.28	3.40	3.44

Figure 6. Implications of Kapβ2 binding to multiple sites across FUS: SAXS analysis and RNA-binding

A) SAXS profiles of MBP, MBP-FUS, Kapβ2, Kapβ2•FUS, and Kapβ2•MBP-FUS produced radius of gyration R_g^{SAXS}, maximum particle size D_{max}, and pair distribution function P(r). $R_g^{Globular}$ was estimated using the formula of $6.6*MW^{0.333}$ Å. Right, *ab initio* shapes of MBP-FUS and Kapβ2•FUS with the structures of MBP (PDBID **1Y4C**), Kapβ2 (PDBID **2QMR**), and the FUS PY-NLS (Figure S2F, G) coarsely fitted to the SAXS envelopes. See also Figure S6 and Table S4. **B)** Size exclusion chromatography (monitored by $Abs_{280\ nm}$, $Abs_{260\ nm}$ and fluorescence emission at 520 nm ($Em_{520\ nm}$)) of 1 μM prD RNA alone and 1 μM prD + 3 μM MBP-FUS (left), and of 1 μM prD + 3 μM MBP-FUS+3.2 μM Kapβ2 (right). **C)** Size exclusion chromatography as in **B)** of 2 μM TERRA RNA alone and 2 μM TERRA + 3 μM MBP-FUS (left), and 2 μM TERRA + 3 μM MBP-FUS + 3.2 μM Kapβ2 (right). 5′ of the RNAs were labeled with 6-FAM fluorophore and proteins were visualized by Coomassie blue stained SDS/PAGE.

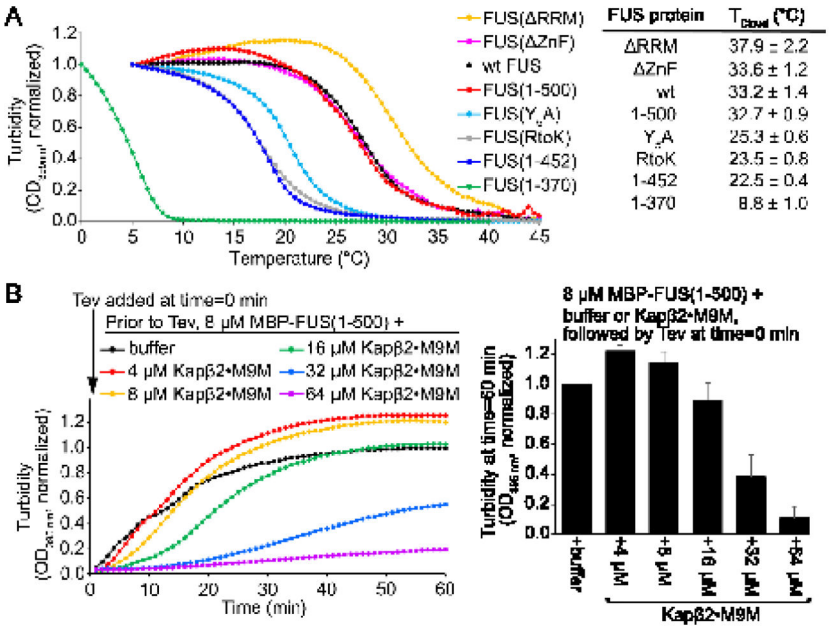

Figure 7. Regions of FUS that bind Kapβ2 contribute to phase separation

A) Temperature dependence of FUS phase separation. Turbidity (OD_{395nm}) of 8 μM MBP-FUS proteins (wildtype (wt) and FUS mutants) after 3 h treatment with Tev protease was monitored as temperatures were decreased from 40°C or 45°C to 0°C or 5°C. Optical densities were normalized to values measured at 0°C or 5°C. T_{Cloud} is the x-intercept of tangent at inflection point of the curve (mean of 3 technical replicates, ± S.D.). **B)** Left, turbidity of 8 μM MBP-FUS(1–500), in the presence of buffer or 4–64 μM Kapβ2•M9M, measured for 60 min at room temperature after treatment with Tev protease. Right, turbidity at time=60 min of experiments in the left panel, normalized to FUS turbidity in the presence of buffer (mean of 3 technical replicates, ± S.D.). See also Figure S7.